processes

MDPI

Article

Dynamic Characteristics of Large-Size Substrates in Magnetron Sputtering Systems

Le Huang [1,2], Qiancheng Zhao [1,*], Congfang Hu [3], Xian Wang [1] and Siyuan Liu [3]

[1] College of Mechanical and Electrical Engineering, Hunan University of Science and Technology, Xiangtan 411201, China; huangle@hdzk.com.cn (L.H.)
[2] Xiangtan Hongda Vacuum Technology Co., Ltd., Xiangtan 411104, China
[3] School of Mechanical Engineering and Mechanics, Xiangtan University, Xiangtan 411105, China
* Correspondence: qczhao@hnust.edu.cn

Abstract

Large-size substrates (G10.5, 3370 mm × 2940 mm × 0.5 mm) are increasingly employed in magnetron sputtering, and their dynamic behavior—defined as the vibration-induced displacement, velocity, and acceleration responses of the panel during movement—exerts a strong influence on coating quality. Nevertheless, the dynamic behavior of substrates at the G10.5 scale has yet to be examined, leaving no quantitative basis for selecting an appropriate substrate movement configuration. To address this gap, two substrate movement modes, a carrier-free tilt mode and a permanent-magnet-constrained vertical mode, were developed and compared, with the aim of quantifying their dynamic performance and establishing a direct mode-selection criterion. The maximum allowable tilt angle was determined theoretically, while the magnetic force was evaluated by the magnetic charge integration method. ABAQUS was subsequently used to extract the first six natural frequencies, and the forced-vibration responses were computed through modal superposition. A tilt angle of 6° is recommended: relative to 0°, the Z-direction displacement amplitude and peak-to-peak value were reduced by 37.57% and 21.05%, respectively. The vertical mode reduced the overall response amplitude by 15.8% relative to 0° (and by 3.47% relative to 6°), although on the coating-critical Z-direction component, it remained approximately 51% higher than the 6° tilt mode, because the magnetic constraint primarily suppresses the lateral X- and Y-responses. The 6° tilt mode is therefore recommended for coating-uniformity-critical applications, whereas the vertical mode is preferred where lateral positional stability is the dominant requirement.

Keywords: magnetron sputtering; large-size substrate; dynamic analysis; tilt mode; vertical mode; magnetic attraction constraint

Check for updates

Academic Editor: Salvador Tututi-Avila

Received: 21 October 2026
Revised: 18 November 2026
Accepted: 24 November 2026
Published: 27 November 2026

Copyright: © 2026 by the authors. Licensee MDPI, Basel, Switzerland. This article is an open access article distributed under the terms and conditions of the Creative Commons Attribution (CC BY) license.

1. Introduction

Magnetron sputtering coating technology has been extensively developed in recent years owing to its advantages of high film density, strong adhesion, high deposition efficiency, and a low thermal load on the substrate [1]. It has consequently found wide application in display manufacturing [2,3], optical and functional oxide coatings [4–8], microelectronics and magnetic devices [9], biomedical devices [10–12], mechanical and wear-resistant engineering [13–15], and radiation-resistant materials [16]. With rapid advances in digital technologies, the demand for transparent conductive glass in display applications has grown substantially. To meet the requirements of higher production throughput and larger glass substrates, continuous magnetron sputtering systems have been developed.

These systems generally adopt a multi-chamber configuration that permits continuous, sequential film deposition, and each deposition chamber contains the magnetron sputtering targets together with a substrate transport system operating under vacuum.

Continuous deposition systems are generally classified into vertical and tilt configurations. Among these, vertical transport systems are widely employed for the double-sided deposition of transparent conductive glass owing to their structural advantages and process flexibility, and they have therefore attracted considerable research attention. Several studies [14,15,17] used magnetron sputtering to prepare multilayer, ceramic and metallic film systems and examined the influence of deposition parameters on film microstructure and compositional uniformity. Yurjev et al. [18] deposited superconducting films on sapphire substrates by magnetron sputtering, and optimization of the substrate interface conditions and deposition parameters markedly improved the resulting coating quality.

In addition to vertical deposition systems, attention has increasingly turned to tilt deposition configurations. Several studies [19–22] employed magnetron sputtering to deposit films of various materials on tilt substrates, correlating experimental observations with simulated distributions of particle energy and incidence angle. Through systematic analysis of film morphology and properties, uniform coating coverage was achieved.

In continuous magnetron sputtering systems, substrates are moved by a carrier mechanism to sustain a continuous coating process. To enhance coating quality and deposition efficiency, considerable research efforts have been devoted to substrate transport systems and motion control strategies across a range of substrate configurations. Huang et al. [23] proposed a planetary-motion sputtering system for preparing laterally graded multilayer films and developed a film thickness distribution model that accounts for the transport characteristics of fast and slow sputtered particles: fast particles are energetic atoms that travel ballistically from the target with little energy loss, whereas slow particles are thermalized atoms that undergo repeated collisions and reach the substrate mainly by diffusion. Several studies [24,25] established three-dimensional numerical models of magnetron sputtering with rectangular or cylindrical targets and showed that the decay of the edge magnetic field leads to non-uniform target erosion; optimizing the magnetic field displacement substantially improved the erosion uniformity. Other investigations explored alternative substrate motion strategies, in particular rotational motion, to improve film uniformity. Mathematical models of rotational and planetary-motion systems have been developed and demonstrate that adjusting the rotation speed reduces surface roughness and grain size while modulating resistivity and microstructure, thereby markedly improving the thickness uniformity of the deposited films [26–28]; comparable benefits under rotating kinematics have also been reported for atmospheric plasma spraying [29].

Several studies [30–32] explored the use of shadow masks to improve film deposition uniformity. The results demonstrated that shadow masks enable precise thickness control while preserving the interfacial structure, surface morphology, and optical properties of the coating. Building on this approach, Li et al. [33] introduced a shielding mask between the substrate and target to selectively modify the deposition plume, achieving precise thickness regulation and improved film quality. This method offers advantages in fabrication simplicity, cost-effectiveness, operational flexibility, reliability, and durability.

Beyond in-chamber motion strategies, the handling and transfer of large glass substrates between and within vacuum tools have been investigated mainly from a robotics perspective. Liu et al. [34] developed a high-speed handling robot with a bionic end-effector for large glass substrates in clean environments and characterized its positioning error and end-effector vibration. Shan et al. [35] identified a linear state-space model of the end-effector of a glass-substrate transfer robot and suppressed its low-frequency vibration using a linear-quadratic-Gaussian controller. Liu and Chen [36] combined S-curve feed rate profiling

with input shaping to attenuate the residual vibration of glass-substrate transfer robots, while Seo et al. [37] analyzed LCD transfer robots through coupled dynamic simulation and experiment. These studies, however, addressed robotic handling between process tools rather than the dynamic behavior of the substrate itself during in-chamber movement, which has not been examined at the G10.5 scale.

Existing research has focused primarily on optimizing deposition processes and substrate motion strategies to improve coating uniformity. As transparent conductive glass substrates continue to increase in size, however, simply scaling up conventional transport systems may compromise movement stability and restrict industrial applicability. To address this challenge, the specific objective of this study is to propose two substrate movement modes—the tilt mode and the vertical mode—and to conduct a comparative force analysis of the two configurations. On the basis of free and forced vibration analyses, the dynamic responses of the two modes were evaluated: the vertical mode was found to suppress the overall and lateral (X/Y) responses more effectively, whereas the optimized tilt mode provides better control of the coating-critical out-of-plane (Z) response. The vertical mode nevertheless requires additional substrate carrier support and higher installation costs, so the two modes address different precision and cost requirements rather than one being universally superior. These findings offer both theoretical and engineering guidance for the design of large-scale magnetron sputtering transport systems and for practical coating applications.

The novelty of this study is threefold. First, in contrast to previous studies, which have focused predominantly on deposition process optimization and substrate motion strategies, the present work addresses the largely unexplored dynamic behavior of large-size substrates during movement, a factor that becomes increasingly critical as substrate dimensions exceed conventional scales. Second, a carrier-free tilt movement mode is proposed in which the gravitational component normal to the substrate acts as a stabilizing preload: it increases the normal contact force at the supporting rollers and modifies both the geometric stiffness and the load-direction projection of the panel, and the resulting non-monotonic response is quantified by finite-element analysis rather than attributed to added damping. Third, a systematic comparative framework that integrates theoretical force analysis, magnetic force modeling, and finite-element free- and forced-vibration analysis is established to evaluate the dynamic performance of both movement modes quantitatively, providing a direct basis for mode selection according to coating precision requirements.

2. Materials and Methods

This study is founded on the following core assumptions and boundary conditions to ensure the rigor and feasibility of the dynamic analysis. (1) Linear elastic small-deformation assumption: The glass substrate is treated as a homogeneous, isotropic linear elastic material, and the vibration amplitude is far smaller than the substrate dimensions, which lies within the scope of linear structural dynamics. (2) Steady-state harmonic load assumption: The sputtering impact load is represented as a constant-amplitude harmonic excitation to provide a conservative estimate that encompasses the worst-case resonance scenario; the random character of individual particle impacts is examined through a supplementary random response analysis and does not alter the conclusions. (3) Rigid support assumption: The support rollers are defined as analytical rigid bodies with fully constrained translational degrees of freedom, neglecting the micro-deformation of the roller assembly, whose stiffness is orders of magnitude higher than that of the thin glass substrate. (4) Constant magnetization assumption: The permanent magnets operate in a saturated magnetization state under a stable vacuum temperature, and demagnetization is neglected, in accordance with the operating conditions of industrial magnetron sputtering systems. (5) Constant

modal damping assumption: A uniform modal damping ratio of 0.05 is adopted, accounting for both the material damping of the glass and the interfacial energy dissipation at the roller–substrate contact.

The modal superposition method is selected for the forced-vibration analysis because the first two modes account for more than 95% of the total modal effective mass in this large-size thin-plate structure. The method combines high computational efficiency with sufficient engineering accuracy and is widely applied in the steady-state dynamic analysis of thin-plate structures.

2.1. Vertical and Tilt Modes for Substrate Movement

Figure 1a illustrates the operating principle of the magnetron sputtering production line and the layout of the coating chamber. In conventional continuous magnetron sputtering systems, substrate movement is generally realized through either a driven-wheel constraint mode or a magnetic constraint mode, and the principal difference between them is whether a substrate carrier is employed. Although such a carrier enhances coating stability, it requires the substrates to be mounted on the carrier and consequently occupies considerable installation space. For large-size substrates, this requirement substantially lowers production efficiency, while the carrier itself also increases equipment cost and system complexity. In contrast, the proposed tilt movement mode removes the need for a substrate carrier, thereby reducing both spatial requirements and overall system cost.

In this configuration, the driving wheel is equipped with an adjustable tilt mechanism that allows its tilt angle to be modified in accordance with the loading conditions, and the substrate is consequently moved at a prescribed tilt angle relative to the horizontal plane. The normal component of gravity acting on the substrate increases the preload at the roller–substrate contacts, which modifies the geometric stiffness and the projection of the applied load relative to the panel and thereby stabilizes the substrate. Driving power is supplied by the lower driving wheel assembly, whereas the upper assembly, comprising the driven wheel and driven shaft, provides support and guidance. Together, the lower and upper assemblies establish a stable vertical transport plane, as illustrated in Figure 1b.

During substrate movement, the stability of large-size substrates is governed primarily by impact loads and structural vibrations. To provide a benchmark against which the proposed tilt movement mode could be evaluated, a conventional vertical transport system with magnetic constraints was established, as shown in Figure 1c. In this system, the substrate is mounted on a carrier that provides structural support throughout the transport process. The carrier is propelled by a set of driving wheels installed at the lower end, while permanent magnets positioned at the upper end generate non-contact positioning constraints through magnetic coupling. This configuration continuously constrains the substrate carrier in the vertical direction while maintaining precise positioning, thereby ensuring smooth and stable movement.

2.2. Impact Load in the Magnetron Sputtering System

As illustrated in Figure 2, the sputtering process is initiated by the bombardment of the target with argon ions, generating a series of collision cascades within the target material. The transferred kinetic energy propagates through these cascades and, once sufficient energy is accumulated near the surface, target atoms are ejected from the near-surface region.

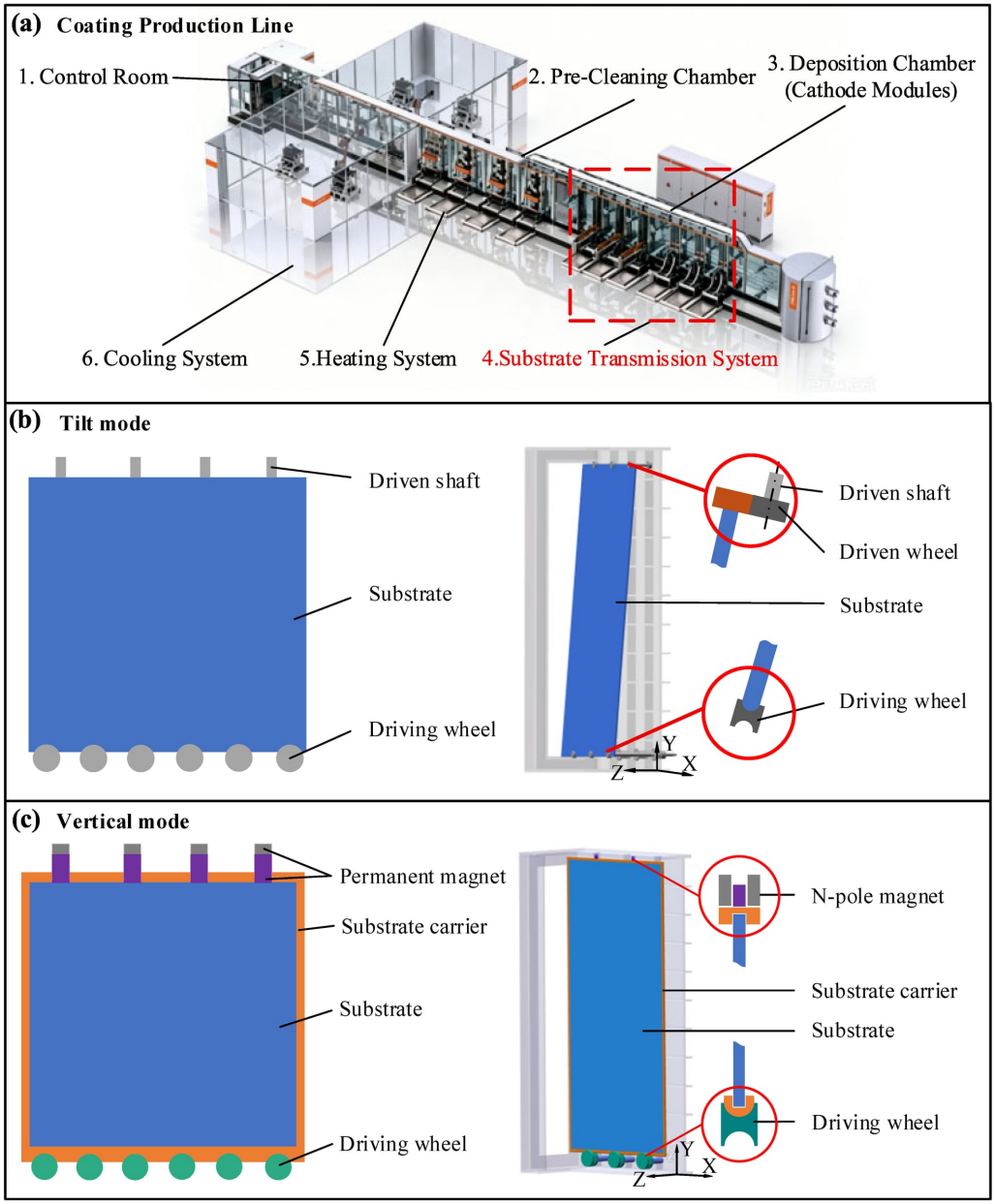


Figure 1. Schematic diagrams of the two proposed movement modes for a large-size substrate in the magnetron sputtering system: (**a**) overall layout of the continuous coating production line; (**b**) carrier-free tilt movement mode; (**c**) permanent-magnet-constrained vertical movement mode.

The energy of the ejected target atoms, derived from energy conservation, is given by

$$E_0 = E_{Ar} - E_{con} - E_b \tag{1}$$

where E_{Ar} is the energy of positive ions; E_{con} is the binding energy of a target atom; and E_b is the energy loss during the cascade process.

Assuming that the ionization of the working gas occurs predominantly within the cathode sheath and that collisions facilitate complete energy transfer, the kinetic energy of the positive ions impinging on the target under the applied electric field can be expressed as

$$E_{Ar} = qU = q(V_x - V_t) \tag{2}$$

where q is the charge of positive ions; V_t is the cathode voltage; and V_x is the voltage at the position of the positive ion.

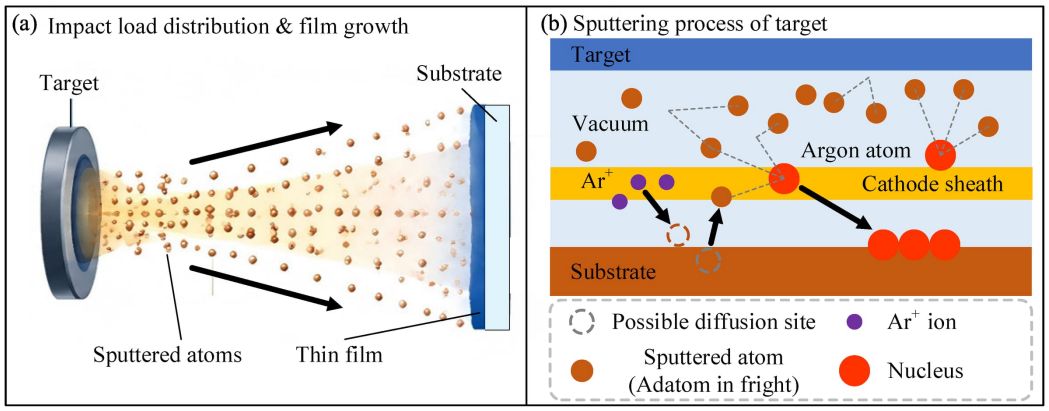


Figure 2. Physical mechanism of the sputtering-induced impact load on the substrate: (**a**) spatial distribution of the equivalent impact load across the deposition zone; (**b**) collision-cascade process of argon-ion bombardment and target-atom ejection at the target surface.

Upon departing the target surface, the energy loss of sputtered atoms is predominantly governed by collisions with the working gas. The corresponding mean free path is given by

$$\lambda_q = \frac{k_b T}{\sqrt{2}\pi d^2 P} \tag{3}$$

where K_b is the Boltzmann constant; T is the operating temperature; d is the molecular diameter of the working gas; and P is the pressure of the gas.

Assuming that the energy required to ionize the working gas remains constant, the energy of the target atoms upon reaching the substrate surface can be calculated by accounting for the cumulative energy loss due to ionization along their flight path. The arrival energy is given by

$$E_{arr} = E_0 - \left(\frac{L}{\lambda_q}\right) E_d \tag{4}$$

where E_{arr} is the kinetic energy of a target atom upon reaching the substrate; E_0 is the atomic energy at ejection from the target (Equation (1)); L is the target-to-substrate flight distance; λ_q is the mean free path (Equation (3)), so L/λ_q represents the number of gas collisions along the path; and E_d is the energy lost in a single ionization event. This relation is derived by the authors from energy conservation.

Upon reaching the substrate surface, the kinetic energy of the target atoms is converted into an impact force through adhesion. Let Δd denote the displacement from initial contact to complete energy dissipation. The resulting impact force exerted on the substrate can be expressed as

$$F_c = \frac{nE_{arr}}{\Delta d} \tag{5}$$

On the basis of the preceding formulae and the parameters listed in Table 1, the impact load is calculated to be 189 N. In magnetron sputtering, however, the applied magnetic field substantially alters the trajectories of charged particles. Ions accumulate locally in the region between the central magnet rod and the surrounding magnetic ring, giving rise to a spatially non-uniform sputtering rate across the target surface. This non-uniformity in turn produces fluctuations in the instantaneous impact load exerted on the substrate. Accordingly, the impact load distribution on large-size substrates can be quantified using a sputter probability density function (Equation (6)), expressed as $F = \Phi \cdot A \cdot m_{\text{atom}} \cdot \Delta v$. It should be emphasized that the value of 189 N represents a cumulative equivalent impact load on the large-size substrate rather than the force exerted by a single atom. Its basis is stated explicitly: for a deposition area of $A = 9.91$ m^2, an arrival flux Φ (on the order

of 10^{15}–10^{17} atoms·cm^{-2}·s^{-1}), a mean atomic mass m_{atom} and a normal velocity change Δv, the steady momentum-flux force is obtained from the momentum balance, and the dissipation distance $\Delta d = 34.7$ nm must be reported for the actual process. Because these quantities are process-dependent, the load magnitude was additionally scaled by 0.5 and 1.5 in Section 3.1.1; the linear solution scales all amplitudes proportionally, while the relative reductions and the recommended configuration remain invariant. The value of 189 N is therefore retained as a conservative nominal equivalent load. In Equation (6), $P(x,y)$ is the sputtering probability density, and B_r and B_z are the radial and axial magnetic flux density components (in T); the proportionality constant is determined by normalizing P over the deposition area so that the integrated probability equals unity.

$$P(x,y) \propto \frac{B_r(x,y)}{{B_r}^2(x,y) + {B_z}^2(x,y)} \tag{6}$$

Table 1. Relevant parameters for magnetron sputtering under impact load.

Meaning	Binding Energy of Target Atom	Cascade Loss of Energy	Gas Molecular Diameter	Target Atom Diameter	Film Thickness	Energy Dissipation
Symbol	E_{con}	E_b	d_g	d_b	h_f	Δd
Value	40 eV	11 eV	0.75 nm	1.72 nm	100 nm	34.7 nm

The theoretically predicted impact load is, however, spatially continuous and inherently non-uniform, which complicates its direct implementation in finite-element software such as ABAQUS 2025. To overcome this difficulty, the continuous distribution was discretized into equal segments and averaged at representative points. Owing to the bilateral symmetry of the sputter probability density (Equation (6)) about the substrate centerline, points A through E listed in Table 2 represent one symmetric half of the deposition zone: the sputtering yields sum to approximately 50% and the corresponding force magnitudes to 92.5 N. An identical, mirror-symmetric set of loads is applied to the other half of the substrate in the finite-element model and is omitted from Table 2 for brevity. The total load applied in the model, approximately $2 \times 92.5 = 185$ N, is thus consistent with the theoretical cumulative value of 189 N; the small discrepancy of about 2% results from the rounding of segment-averaged values. The impact-load distribution curves over the large-area substrate are presented in Figure 3, and the load magnitudes at points A to E are summarized in Table 2; these results are used in the subsequent simulations.

Table 2. Discretized impact load magnitudes at points A–E (one symmetric half of the deposition zone).

Sign	*A*	*B*	*C*	*D*	*E*
Sputtering yield (%)	6.35	10.58	15.08	14.29	3.70
Force(N)	12	20	28.5	27	5

2.3. Deflection of the Tilt Large-Size Substrate Under Gravity

In tilt movement systems for large-size substrates, driven wheels are commonly employed to provide mechanical support and positional constraint. However, the tilt configuration alone cannot fully guarantee substrate stability during operation. The instability of large-size substrate movement is primarily associated with excessive surface deflection under gravitational loading. To mitigate this issue, the tilt configuration was optimized, in which the gravitational component along the carrier direction partially counteracts the vibration-induced displacement. In the proposed system, the lower end of the tilt movement structure is equipped with driving shafts and wheels to provide power input, whereas the

upper end is supported by driven wheels and shafts. Nevertheless, an excessive tilt angle may increase substrate bending deformation, thereby compromising coating uniformity during film deposition [22]. Therefore, the influence of the tilt angle of the large-size substrate was systematically investigated. As illustrated in Figure 4, increasing the tilt angle gradually increases the gravitational component F_3 acting normal to the substrate at point *C*. Meanwhile, the gravitational component F_4, which acts parallel to the substrate surface, opposes F_2, and consequently reduces its contribution to substrate displacement.

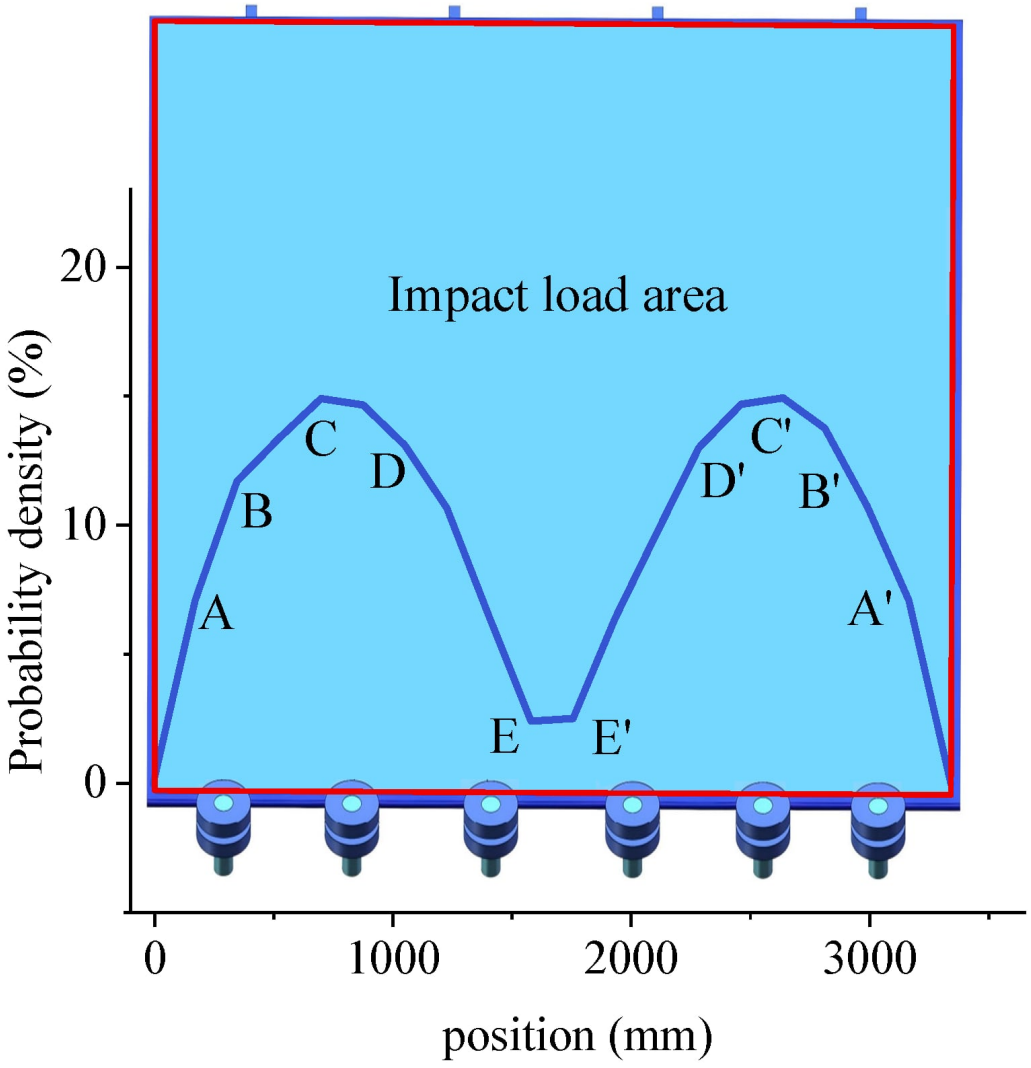


Figure 3. Spatial distributions of the equivalent impact load and the corresponding probabilistic sputtered-particle density over the large-size substrate deposition zone.

Here, *G* denotes the substrate weight, which is decomposed into F_1 and F_2 in the un-tilted configuration; under tilt, *G* is further resolved into F_3 (the component normal to the substrate surface, providing passive damping) and F_4 (the component parallel to the substrate surface, opposing the lateral force F_2).

The deflection of the tilt substrate was calculated using the standard uniformly loaded, simply supported beam relation from elementary mechanics of materials, as follows:

$$\delta = \frac{5Fh^3}{384EI_z} = \frac{5(F_c + G\sin\theta)h^3}{384EI_z} \quad (7)$$

The geometric and mechanical parameters used in the calculation are listed in Table 3.

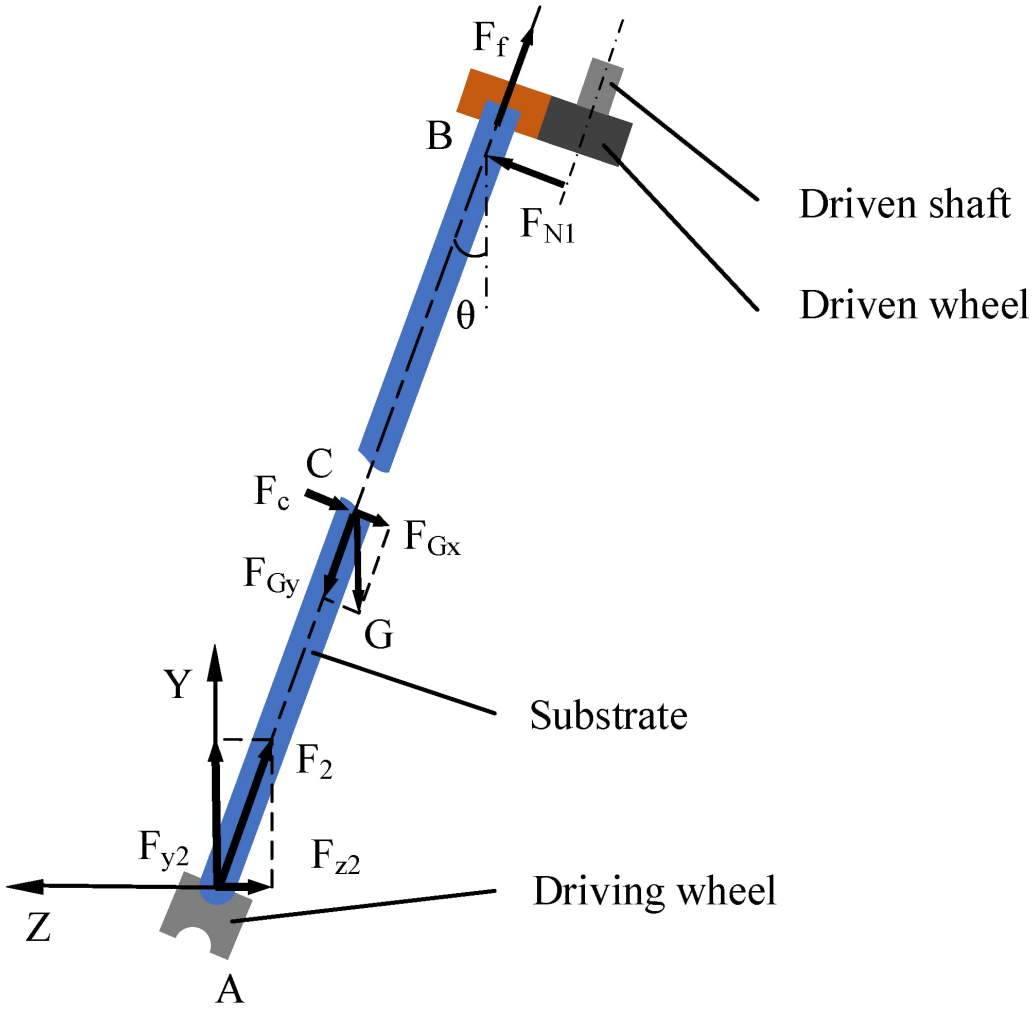


Figure 4. Free-body force analysis of the large-size substrate in the tilt movement mode.

Table 3. Parameters associated with force analysis.

Meaning	The Substrate Length	The Substrate Width	The Substrate Thickness	Structural Gravity	Tilt Angle
Symbol	L	b	t	G	θ
Value	3370 mm	2940 mm	0.5 mm	121.4 N	10.4°

To quantitatively evaluate the substrate bending deformation, the Z-direction displacement data along the left edge of the substrate were extracted and transformed into displacement curves normal to the substrate surface, as shown in Figure 5. The results indicate that an increase in the tilt angle intensifies the bending deformation and raises its rate. When the tilt angle reaches 10.4°, the maximum substrate displacement increases to 0.34 mm. By comparing the simulation results with the theoretical displacement predictions, the maximum allowable tilt angle of the movement system is determined to be below 10°. The value 10.4° is the theoretical angle at which the deflection reaches the 0.34 mm limit and is rounded down to a conservative design limit of less than 10°.

The allowable deflection criterion of 0.34 mm is adopted as an engineering deflection limit for transparent conductive oxide films. Its relation to coating uniformity follows from the target-to-substrate distance d_0: for a thickness distribution scaling approximately as ${d_0}^{-2}$, a gap variation Δd corresponds to a relative thickness variation of approximately $2\Delta d/d_0$,

which must be evaluated for the actual 60mm. SEMI D5 specifies standard substrate sizes and SEMI D15 specifies the surface-waviness measurement method [38,39].

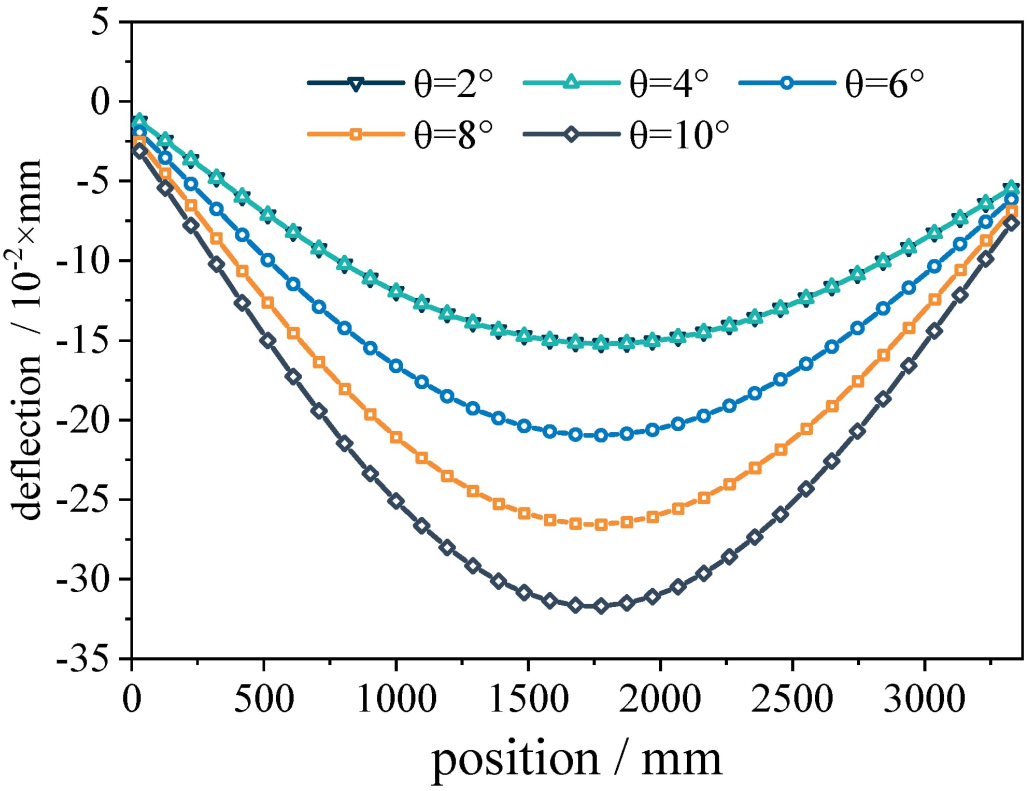


Figure 5. Variation of the substrate normal displacement along the left edge under different tilt angles.

2.4. Magnetic Force Analysis in Vertical Mode

Analysis of the tilt movement system indicates that the driving-wheel constraint alone is insufficient to ensure stable substrate movement. To enhance stability, a vertical transport model incorporating magnetic stabilization was developed, as illustrated in Figure 6. Under magnetic saturation the permanent magnets exhibit a constant magnetization. Accordingly, the magnetic charge integration method was adopted, in which each rectangular permanent magnet is represented by four uniformly distributed pole surfaces for the calculation of the magnetic force.

When magnetic constraints are applied, the upper end of the substrate carrier is stabilized through the magnetic interaction between two permanent magnets in the magnetic attraction positioning system. To quantify this interaction, the magnetic force is calculated based on the magnetization current induced in the magnetically permeable materials, as expressed by the following equation:

$$F = \sum \sum_{V} \sum \delta_V B dV + \iint_{S} \delta_S B dS \tag{8}$$

where

$$\delta_V = \nabla \times M \tag{9}$$

$$\delta_S = -n \times M \tag{10}$$

where the following relations hold: δV is the volume magnetization current density; δS is the surface magnetization current density; B is the magnetic flux density; M is the magnetization of the medium; n is the surface normal vector.

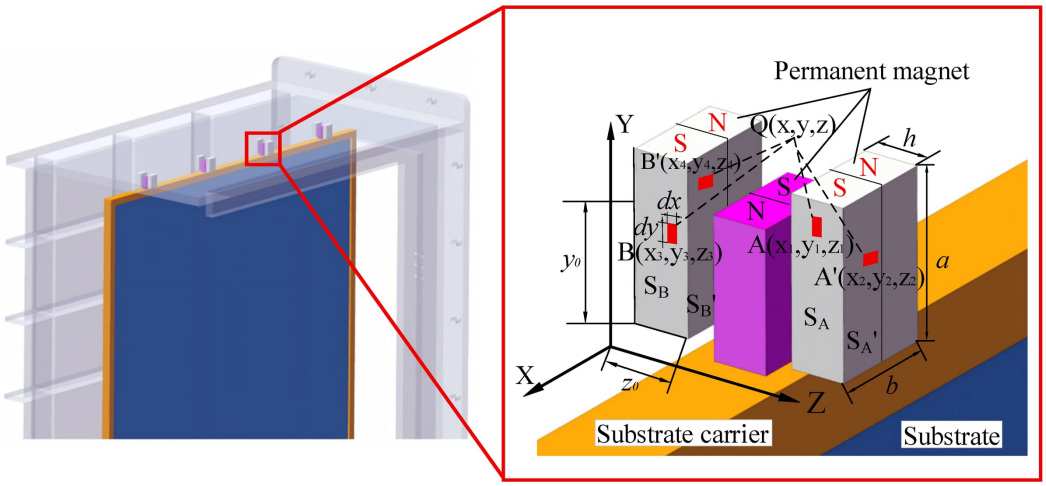


Figure 6. Equivalent magnetic charge distribution model for the rectangular permanent magnets in the magnetic attraction positioning system.

For isotropic media, the magnetic force is expressed as:

The derivation proceeds from the magnetization current density (Equations (9) and (10)) to the equivalent magnetic charge representation, from which the scalar magnetic potential (Equation (13)), magnetic field intensity (Equation (14)), and magnetic flux density (Equations (15) and (16)) are sequentially obtained. The magnetization-current relations (Equations (8)–(12)) provide the physical basis, while the magnetic force was ultimately evaluated using the magnetic charge integration method (Equations (13)–(16)), which is the adopted formulation.

$$F = \iiint_V (\nabla \times M) B dV \tag{11}$$

This can be simplified as follows:

$$F = \frac{1}{2\mu_0} \iint_S B^2 dS = \frac{1}{2\mu_0} B^2 S \tag{12}$$

Under magnetic saturation, the permanent magnet exhibits a constant magnetization. Accordingly, the magnetic charge integration method is employed to model the magnetic field. As illustrated in Figure 6, each rectangular permanent magnet is represented by four uniformly distributed magnetic pole surfaces according to its geometric configuration. The magnetic scalar potential at an arbitrary point Q in space generated by the magnetic pole surfaces can be expressed as follows:

$$\varphi = \iint_{S_A} \frac{\sigma_m}{4\pi\mu_0 r_1} dA + \iint_{S'_A} \frac{\sigma_m}{4\pi\mu_0 r_2} dA' + \iint_{S_B} \frac{\sigma_m}{4\pi\mu_0 r_3} dB + \iint_{S'_B} \frac{\sigma_m}{4\pi\mu_0 r_4} dB' \tag{13}$$

where σ_m denotes the surface magnetic charge density; S_A and S_B represent the N-pole surfaces, while S'_A and S'_B represent the S-pole surfaces; r_i is the distance from the magnetic charge element on the pole surface to the spatial point Q; B_r denotes the remanence flux density of the permanent magnet.

The magnetic field intensity at the spatial point Q generated by the magnetic pole surface can be obtained from the scalar magnetic potential, expressed as

$$H = -\frac{\sigma_m}{4\pi\mu_0} \left(\iint_{S_A} \nabla \frac{1}{r_1} dA + \iint_{S'_A} \nabla \frac{1}{r_2} dA' + \iint_{S_B} \nabla \frac{1}{r_3} dB + \iint_{S'_B} \nabla \frac{1}{r_4} dB' \right) \tag{14}$$

The magnetic flux density at Q is

$$B = \mu_0 \mu_r H + \mu_0 M_0 \tag{15}$$

where μ_r is the permeability of the permanent magnet; M_0 is the magnetization intensity.

According to the magnetic charge integration method, the magnetic flux density between the two rectangular permanent magnets in the magnetic attraction system can be expressed as follows:

$$B = \left(B_x^2 + B_y^2 + B_z^2\right)^{1/2} \quad (16)$$

The key magnetic parameters used in the calculation are summarized in Table 4. According to the above equations, the calculated magnetic force is 200 N. The permanent magnets are designed with dimensions of 80 × 20 × 60 mm, and the magnetic pole spacing d is set to 40 mm. These parameters are substituted into the model, and the magnetic field distribution is analyzed along the symmetry axis of the region between the two magnets in the magnetic attraction positioning system. The variations in magnetic flux density and magnetic force are subsequently obtained, as shown in Figure 7a,b. The results indicate that the magnetic flux density along the symmetry axis initially decreases to a minimum near the midpoint and then gradually increases toward the magnet surfaces. This phenomenon is attributed to the divergence of magnetic flux lines from the magnetic poles, leading to a reduced magnetic field intensity in the central region.

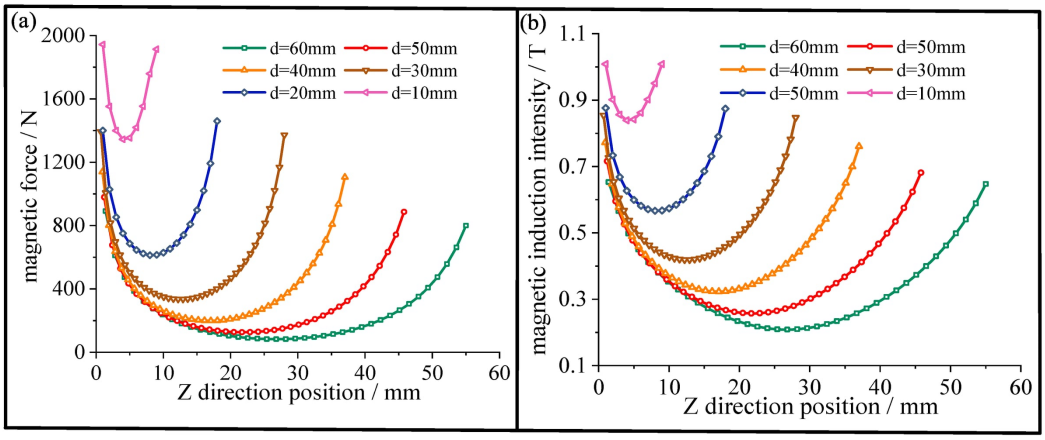


Figure 7. Variation of the magnetic induction intensity and the magnetic force as a function of the separation distance between the paired permanent magnets: (**a**) magnetic induction intensity along the symmetry axis; (**b**) magnetic force between the two magnets.

Table 4. Parameters for magnetic force calculation.

Meaning	Permeability in Vacuum	Magnetic Induction	Effective Contact Area
Symbol	μ_0	B	S
Value	$4\pi \times 10^{-7}$ H/m	0.793 T	8×10^{-4} m^2

The calculated magnetic force of 200 N provides a safety factor of approximately 1.65 relative to the substrate weight of 121.4 N. The total weight of the substrate and carrier assembly should be used for the final design margin; the effective contact area of 8×10^{-4} m^2 corresponds to the 80 mm × 20 mm pole face, and the magnetic induction of 0.793 T should be traced to the magnet grade or remanence, or to measurement or simulation, which are to be reported. The permanent magnets are sintered samarium–cobalt ($SmCo_5$, grade YX-16S) with a remanence flux density (B_r = 0.793 T) at 20 °C, selected for its temperature stability in the vacuum coating.

3. Results and Discussion

3.1. Dynamic Simulation in Tilt Mode

3.1.1. Finite-Element Model of Large-Size Substrate

In this study, finite-element analysis was performed on the substrate movement model. As shown in Figure 8a, the model was discretized using linear hexahedral C3D8R elements, yielding 446,216 nodes and 375,409 elements. A modal-based steady-state dynamic analysis procedure (mode superposition) was employed for the numerical solution. For the contact interaction between the substrate and the rollers, a penalty friction coefficient of $\mu = 0.3$ was defined for the tangential behavior, and the boundary conditions and applied loads are illustrated in Figure 8b. Notably, a damping ratio of 0.05 was used in all subsequent forced-vibration analyses. In the finite-element model for the static and free-vibration analyses, gravity was applied as a static body load, while the six supporting rollers beneath the substrate were constrained during the coating process. For the subsequent forced-vibration analysis, the spatially discretized sputtering impact load (Table 2) was applied as the dynamic excitation, as detailed below.

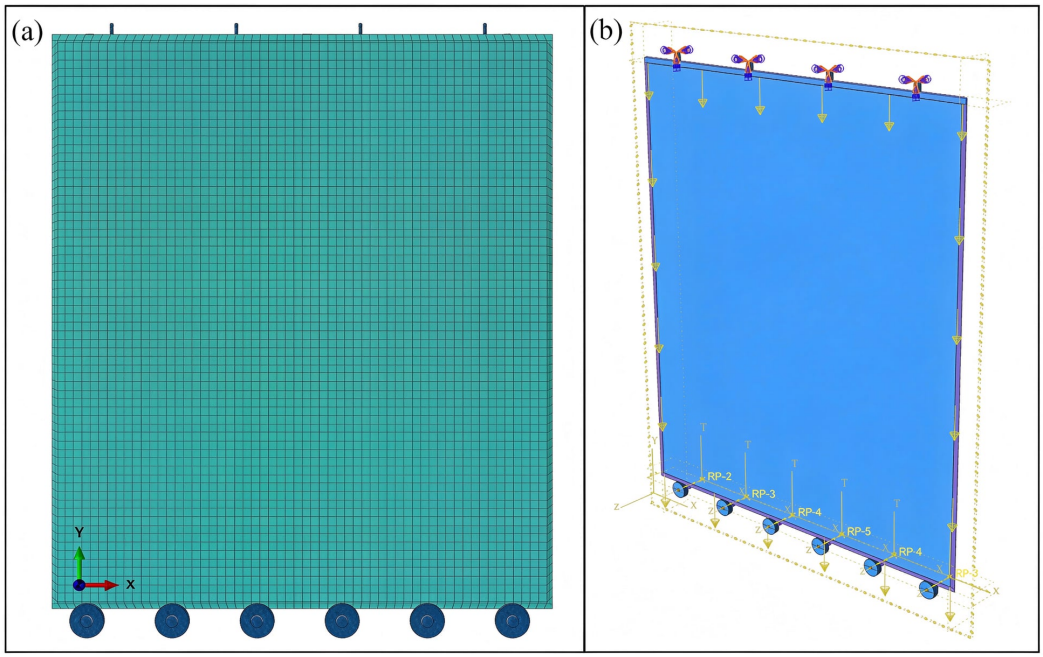


Figure 8. Finite-element simulation model of the large-size substrate movement system: (**a**) discretization using linear hexahedral C3D8R elements; (**b**) applied boundary conditions, support constraints, and dynamic load locations.

Specifically, the six supporting rollers were modeled as rigid analytical bodies, with their translational degrees of freedom fully constrained (U1 = U2 = U3 = 0) while rotational degrees of freedom about the roller axis (UR3) were retained to simulate the driving motion. The three-dimensional geometric model was constructed in SolidWorks2025 and imported into ABAQUS as a STEP file for meshing and analysis.

A mesh independence study was conducted by comparing the first six natural frequencies obtained with three mesh densities: coarse (approximately 180,000 elements), medium (375,409 elements, used in this study), and fine (approximately 720,000 elements). The maximum difference in natural frequencies between the medium and fine meshes was less than 1.2%, confirming that the selected mesh density provides converged results. The C3D8R reduced-integration element was chosen for computational efficiency, and enhanced hourglass control was activated to prevent spurious zero-energy modes. A fric-

tion coefficient of 0.3 was adopted for the glass-steel contact, consistent with experimental measurements reported in the literature for lubricated glass-steel sliding contacts under vacuum conditions. The global element size was approximately 30 mm, with 3 elements through the 0.5 mm thickness, giving an aspect ratio below 3; these values are reported to support reproduction of the mesh.

The forced-vibration analysis was driven by the spatially non-uniform impact load arising from the sputtering process, as described in Section 2.2 and discretized at points *A* through *E* (Table 2). The excitation frequency was mapped from the substrate transport speed: for a typical linear transport speed of 0.5–2.0 m/min, the characteristic passage frequency of the load distribution across the substrate spans 0.05–2.0 Hz, while the broadband impact spectrum from individual particle collisions extends into the low-kilohertz range. The steady-state dynamic analysis was conducted over a frequency range of 0–2000 Hz, encompassing the first six natural frequencies of both movement modes. In this harmonic sweep, the force magnitudes listed in Table 2 define a frequency-independent (constant-amplitude) harmonic force at each load point, and the reported displacement amplitudes correspond to the resonance peaks. This treatment is deliberately conservative: away from the natural frequencies, and particularly across the low-frequency passage band of 0.05–2.0 Hz, the constant-amplitude assumption overestimates the response relative to the physically decaying spectrum of individual impact events. A modal damping ratio of 0.05 was applied uniformly to all modes, in agreement with the typical modal damping values reported in vibration studies of glass-substrate handling systems [34,35]; this damping accounts for the structural material damping and the interfacial energy dissipation at the roller–substrate contacts. The value 0.05 is an effective modal damping that includes roller–substrate interfacial dissipation, whereas the intrinsic glass damping is lower (about 0.1–1%), and the 0.03–0.07 sensitivity range reported below bounds the effective value. The reported resonance peaks represent upper bounds, because the operational passage band (0.05–2.0 Hz) lies below the first natural frequency.

To account for the random character of individual particle impacts, a supplementary modal-based random-response analysis was conducted using a band-limited, approximately uniform power spectral density (PSD) derived from the total equivalent load over 0–2000 Hz. The resulting root-mean-square (RMS) displacements preserve the same ranking as the harmonic results: the vertical mode reduces the overall RMS displacement by approximately 15% relative to the tilt mode at 0° and by about 3% relative to the tilt mode at 6°, while the Z-direction RMS displacement is reduced by roughly 6%, and the minimum tilt-mode response again occurs at 6°. The close agreement between the harmonic and PSD results confirms that the conclusions are governed by the modal characteristics rather than by the excitation-spectrum assumption; the more conservative harmonic values are therefore retained as the principal results.

The three-dimensional model of the large-size substrate movement system comprises two distinct material types. The substrate is made of glass, while the remaining structural components are fabricated from 45 steel (equivalent to AISI 1045) to ensure sufficient mechanical strength and structural rigidity. The key material properties, including density, Young's modulus and Poisson's ratio, are summarized in Table 5. These material parameters were assigned within the ABAQUS model to characterize the mechanical behavior of each component and to provide a reliable basis for the subsequent finite-element analyses of the system's dynamic responses under no-load conditions.

A brief sensitivity analysis was conducted to assess the robustness of the simulation results with respect to the key modeling assumptions. The penalty friction coefficient was varied between 0.2 and 0.4, and the resulting variation in the first six natural frequencies was below 3.2%, indicating that the modal characteristics are not highly sensitive to the friction

coefficient within the physically reasonable range for glass–steel contact. The damping ratio was varied from 0.03 to 0.07, which altered the forced-vibration response amplitude by approximately ±8.5%, while the optimal tilt angle of 6° remained unchanged. The discretization of the spatially non-uniform impact load into five equal segments introduces an averaging error estimated to be below 5% relative to a finer ten-segment discretization. The boundary condition simplification, which treats the six supporting rollers as fixed supports, neglects the minor compliance of the roller assemblies; however, because the roller stiffness is orders of magnitude higher than that of the thin glass substrate, this simplification has a negligible effect on the substrate-dominated vibration modes. These results confirm that the principal conclusions regarding the optimal tilt angle and the relative performance of the two movement modes are robust to reasonable variations in the modeling assumptions.

Because the cumulative load of 189 N is a conservative upper-bound estimate, its magnitude was additionally scaled by factors of 0.5 and 1.5 to test the sensitivity of the conclusions to the load level. For the linear elastic, modal-based solution, all displacement, velocity, and acceleration amplitudes scale in direct proportion to the applied load, whereas the natural frequencies, mode shapes, the optimal tilt angle of 6°, and the relative margins between configurations remain unchanged (Table 6). The overall reductions of 15.8% relative to 0° and 3.47% relative to 6°, together with the Z-direction reduction of 5.92%, are thus invariant to the load level, demonstrating that the mode-selection conclusions do not reverse over a ±50% uncertainty in the impact-load magnitude.

To ensure the reliability and reproducibility of the simulation results, systematic verification and sensitivity analyses were carried out.

(1) Mesh independence verification: Three mesh densities were designed, namely, coarse (about 180,000 elements), medium (375,409 elements, adopted in this study) and fine (about 720,000 elements). The maximum difference in the first six natural frequencies between the medium and fine meshes is below 1.2%, indicating that the selected mesh has converged. The global element size is 30 mm, three elements are arranged through the 0.5 mm thickness, the element aspect ratio is below 3, and the C3D8R reduced-integration element with enhanced hourglass control is selected for its balanced accuracy and efficiency in thin-plate bending problems.

(2) Parameter sources: The glass properties are taken from standard float glass material manuals, and the 45 steel (AISI 1045 [40]) properties from standard mechanical engineering material databases. The friction coefficient of 0.3 for glass–steel contact under vacuum is consistent with experimental measurements in the published literature, and the modal damping ratio of 0.05 is taken from published vibration studies of glass substrate handling systems, including the interfacial dissipation at the contact interface.

(3) Sensitivity analysis: When the friction coefficient varies from 0.2 to 0.4, the natural-frequency variation is below 3.2%; when the damping ratio varies from 0.03 to 0.07, the forced-vibration amplitude changes by about ±8.5%, while the optimal tilt angle of 6° remains unchanged. The five-segment discretization of the impact load introduces an error below 5% relative to a ten-segment discretization. These results demonstrate that the conclusions are robust within reasonable parameter ranges.

(4) Load scaling verification: When the total impact load is scaled by factors of 0.5 and 1.5, all displacement amplitudes scale proportionally, whereas the optimal tilt angle and the relative performance ranking of the two configurations remain unchanged, as shown in Table 6.

Table 5. Material parameters used in the simulation analysis.

Material	Density (kg/m^3)	Young's Modulus (GPa)	Poisson's Ratio
glass	2500	72	0.2
45 steel	7850	206	0.3

Table 6. Normalized forced-vibration displacement amplitudes under scaling of the impact-load magnitude (normalized to the nominal 1.0-factor case).

Load Factor	Tilt 0°, Overall	Tilt 6°, Overall	Vertical, Overall	Tilt 0°, Z	Vertical, Z	Optimal Angle
0.5	0.50	0.50	0.50	0.50	0.50	6°
1.0	1.00	1.00	1.00	1.00	1.00	6°
1.5	1.50	1.50	1.50	1.50	1.50	6°

3.1.2. Gravity-Induced Deflection of the Large-Size Substrate

Figure 9 illustrates the displacement distribution of the large-size substrate under different tilt angles under gravitational loading. The results reveal that increasing the tilt angle intensifies the non-uniform bending deformation of the substrate. Specifically, the displacement in the Y-direction gradually decreases, whereas the maximum Z-direction displacement increases. This indicates that the substrate bending deformation is mainly concentrated along the Y and Z directions.

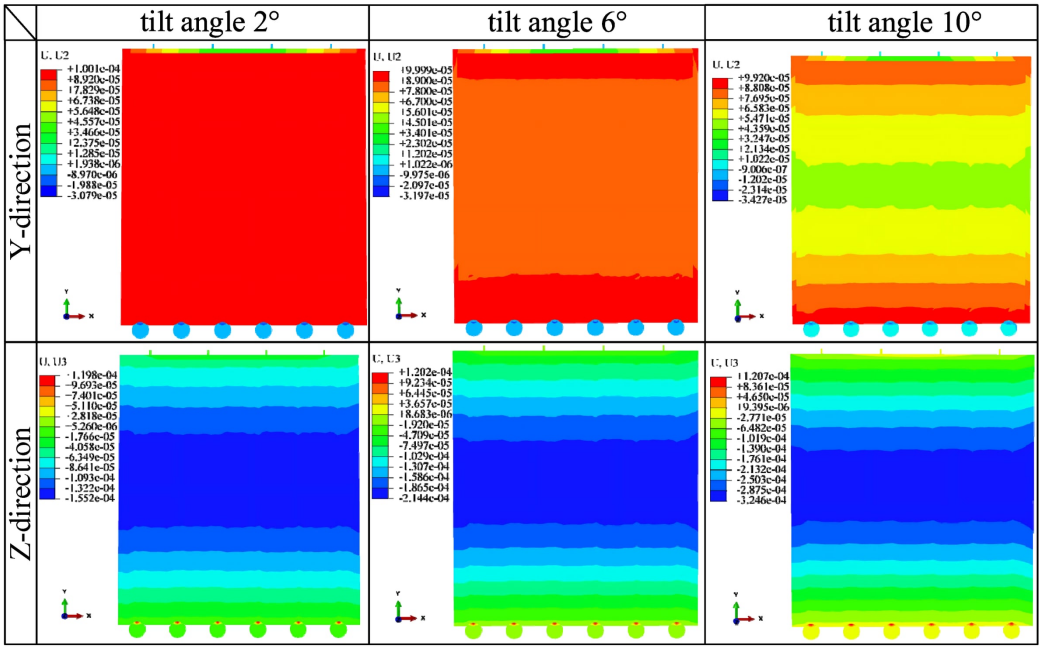


Figure 9. Gravity-induced displacement distributions of the large-size substrate at different tilt angles.

The maximum deflection magnitude along the Z-axis was extracted from the finite-element analysis results presented in Figure 9. A comparison between these simulated maximum deflections and the corresponding theoretical predictions established in this study is presented in Figure 10. The results demonstrate good agreement between the theoretical predictions and the numerical simulations, with consistent variation trends observed for both datasets. Furthermore, the maximum relative error is less than 7%, which is within an acceptable engineering tolerance. These results validate the theoretical model and demonstrate its capability to accurately predict the maximum substrate deflection.

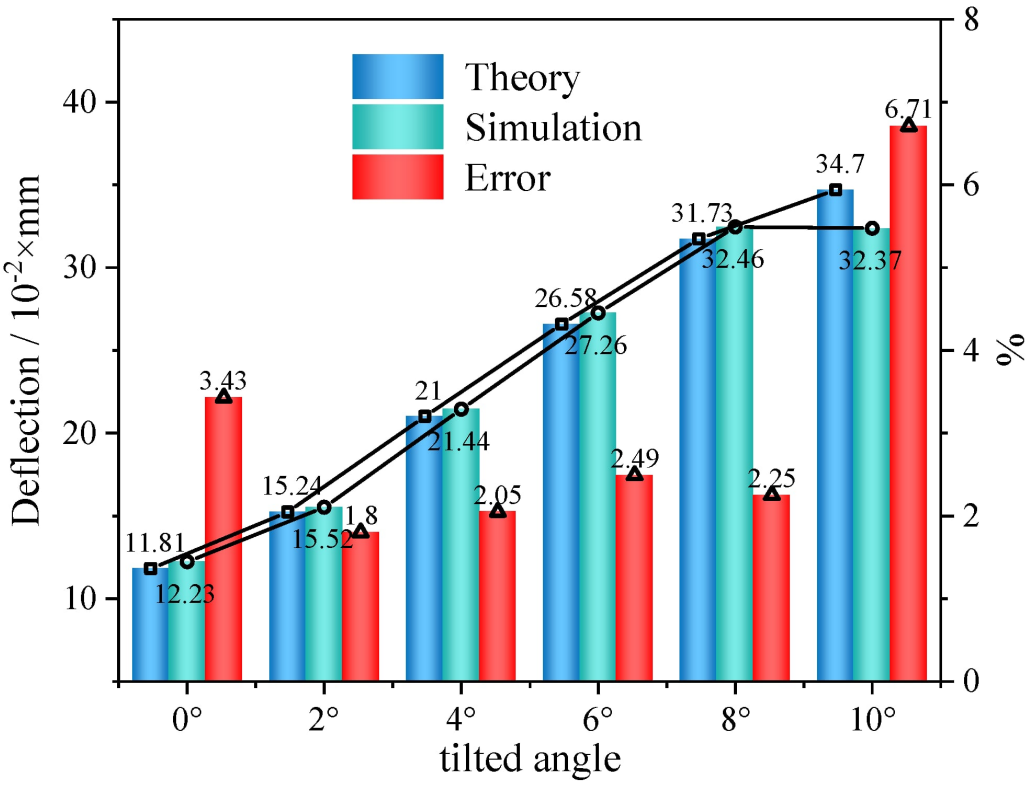


Figure 10. Comparison between the theoretical predictions and the finite-element simulation results for the maximum substrate deflection under gravity as a function of the tilt angle.

3.1.3. Free-Vibration Frequency Analysis of the Large-Size Substrate

Based on the tilt model shown in Figure 1b, the three-dimensional movement system model was imported into ABAQUS for finite-element analysis. Following the application of the corresponding loads and boundary conditions, a modal analysis was conducted to determine the inherent dynamic characteristics of the system, and the first six natural frequencies under free vibration are summarized in Table 7.

Table 7. The first six natural vibration frequencies of the large-size substrate in tilt mode.

Order	1	2	3	4	5	6
Frequency (Hz)	22.84	179.91	564.73	644.31	949.41	1281.4

Figure 11 illustrates the overall vibration modes of the movement system at a tilt angle of 6°. The vibration characteristics change markedly as the mode order increases. In the first- and second-order modes the displacement exhibits a regular horizontal wave pattern, whereas with increasing mode order the patterns become progressively complex and irregular, accompanied by more pronounced displacement variations. In particular, the fourth- and fifth-order modes display distinct elliptical regions of relatively large displacement. A comparison across the mode orders further reveals that, in the lower-order modes, the overall vibration is concentrated mainly in the upper and middle regions of the movement system; as the mode order increases, the dominant vibration distribution gradually shifts from a horizontal to a vertical pattern.

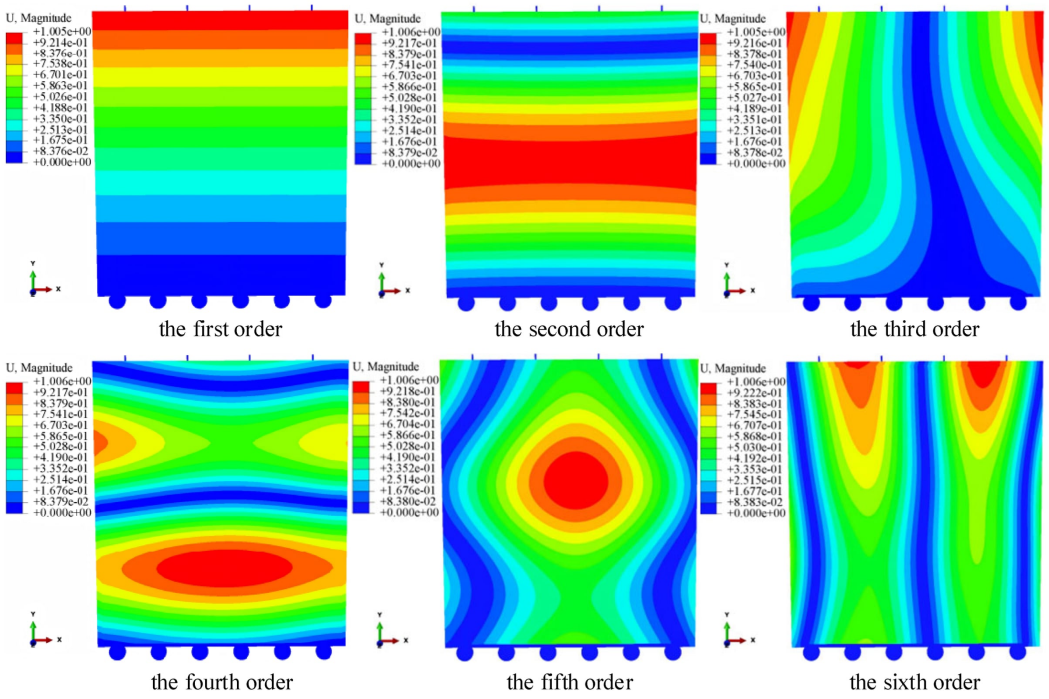


Figure 11. The first six overall free-vibration mode shapes of the large-size substrate movement system at the optimal tilt angle of 6°.

Figure 12 shows the first-order vibration mode of the large-size substrate at tilt angles ranging from 0° to 10°. In the first-order mode, the substrate exhibits a predominantly vertical displacement pattern at all tilt angles, with deformation gradually increasing from the lower end to the upper end. As the tilt angle increases, the overall mode shape remains essentially unchanged. Among the three directional components (X, Y, Z), the component in the Z-direction dominates the modal response, whereas the X- and Y-direction modes exhibit no significant variation. Therefore, the subsequent analysis focuses on the Z-direction vibration mode.

Movement instability may cause the large-size substrate to tilt during movement. To evaluate the influence of substrate tilt on the modal characteristics, the Z-direction vibration displacement was extracted for further analysis. On the basis of the Z-direction vibration displacement distributions of the first six modes, the displacement curves along the upper edge of the substrate, perpendicular to the carrier direction, were obtained, as shown in Figure 13. The marks A, B, C and D in Figure 13 correspond to the respective positions labeled on the substrate in Figure 3.

The Z-direction vibration mode analysis indicates that the displacement distributions vary considerably among different tilt angles in the lower-order modes, whereas their overall variation trends remain consistent. In addition, as the tilt angle increases, the displacement amplitude along the upper edge of the substrate gradually increases, indicating enhanced out-of-plane vibration. Except for the second-order mode, the displacement along the upper edge remains relatively small. At a tilt angle of 6°, however, the fifth- and sixth-order modes exhibit distinct abrupt changes in the vibration displacement curves, indicating a noticeable alteration in the modal deformation characteristics.

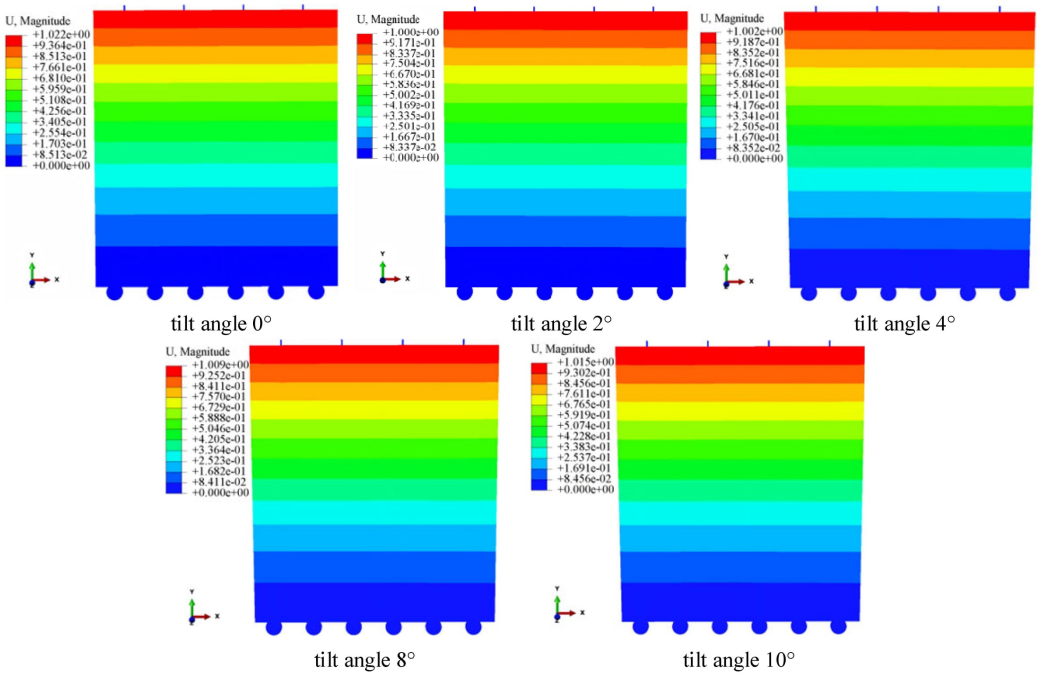


Figure 12. The first-order overall free-vibration mode shape of the large-size substrate at tilt angles ranging from 0° to 10°.

3.1.4. Forced-Vibration Analysis of the Large-Size Substrate

Modal superposition analysis based on the first six free-vibration modes, including their natural frequencies and mode shapes, showed that the modal effective mass of the movement system is highly concentrated in the first two modes (Table 8). The first mode makes the largest contribution, followed by the second mode; together, these two modes account for more than 95% of the total modal effective mass, while the contributions of modes 3 to 6 are negligible. This distribution characteristic remains consistent across all the investigated tilt angles, with no appreciable variation in the relative fractional contributions.

Table 8. Modal effective mass proportion at each tilt angle.

Order	Effective Mass Proportion (%)					
	0°	2°	4°	6°	8°	10°
1	77.81	77.8	77.80	77.79	77.79	77.78
2	17.64	17.63	17.63	17.63	17.63	17.62
3	0.02	0.02	0.02	0.02	0.02	0.02
4	4.01	4.02	4.02	4.02	4.03	4.04
5	0.52	0.53	0.53	0.53	0.53	0.54
6	<0.01	<0.01	<0.01	<0.01	<0.01	<0.01

Using the modal superposition method described above, the displacement distributions of the large-size substrate at different tilt angles were obtained, as illustrated in Figure 14. As the movement tilt angle increased, the overall displacement distributions remained similar, with their magnitudes governed primarily by the dominant horizontal bending mode and exhibiting an upward curvature. The displacement amplitude nevertheless displayed a non-monotonic trend with increasing tilt angle, reaching a minimum at 6° and increasing thereafter.

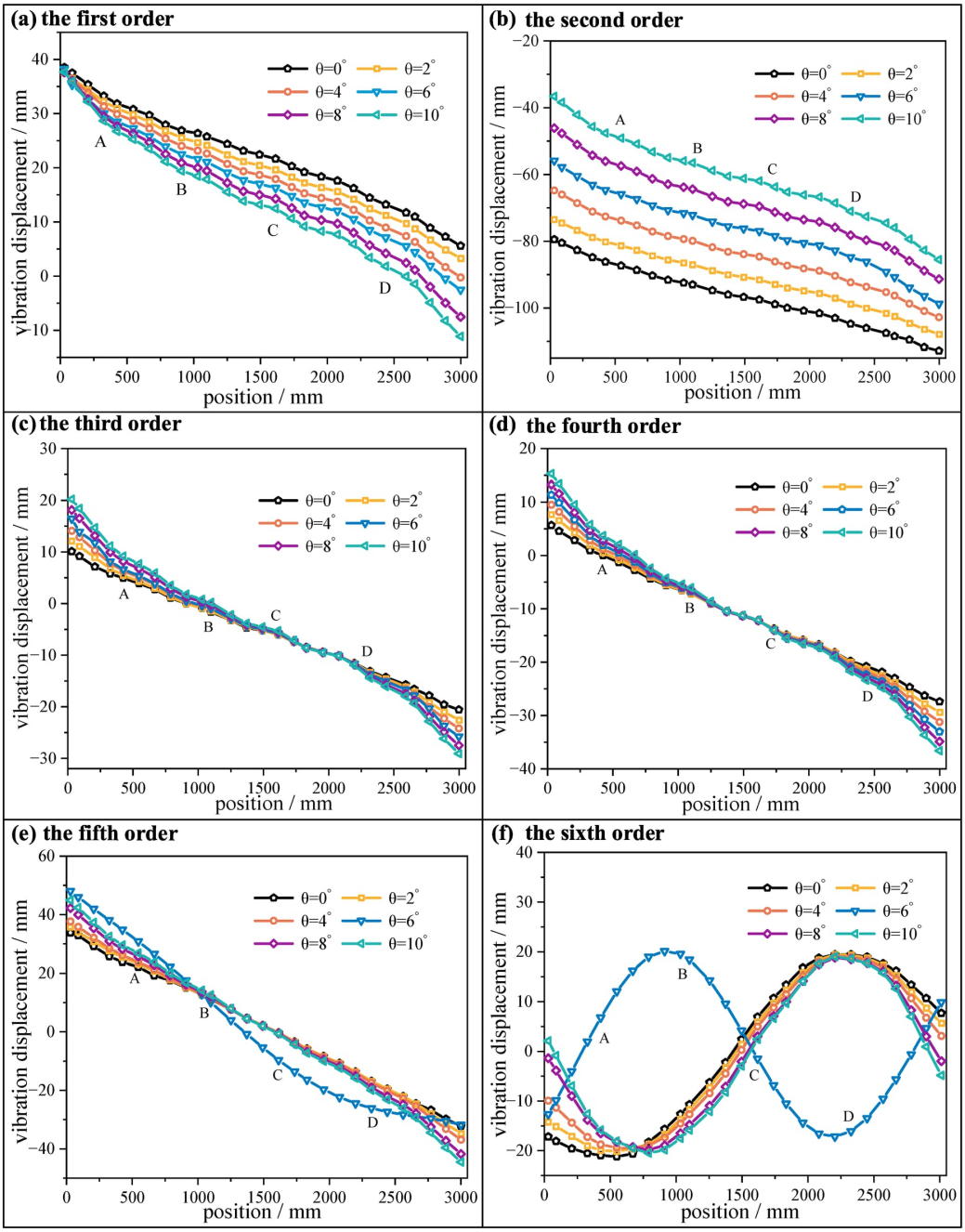


Figure 13. Z-direction vibration displacement distributions along the upper edge of the substrate for the first six free-vibration modes: (**a**) first mode, (**b**) second mode, (**c**) third mode, (**d**) fourth mode, (**e**) fifth mode, and (**f**) sixth mode, highlighting the abrupt modal veering at 6° in the fifth and sixth modes.

Across all investigated tilt angles, the X- and Y-direction displacement distributions obtained by the modal superposition method remained nearly unchanged in their spatial patterns: the X-direction response exhibited a vertical distribution, whereas the Y-direction response displayed a horizontal pattern. Figure 15 shows the representative results at the optimal tilt angle of 6 degrees. The displacement amplitudes in the two directions showed only minor differences at all tilt angles.

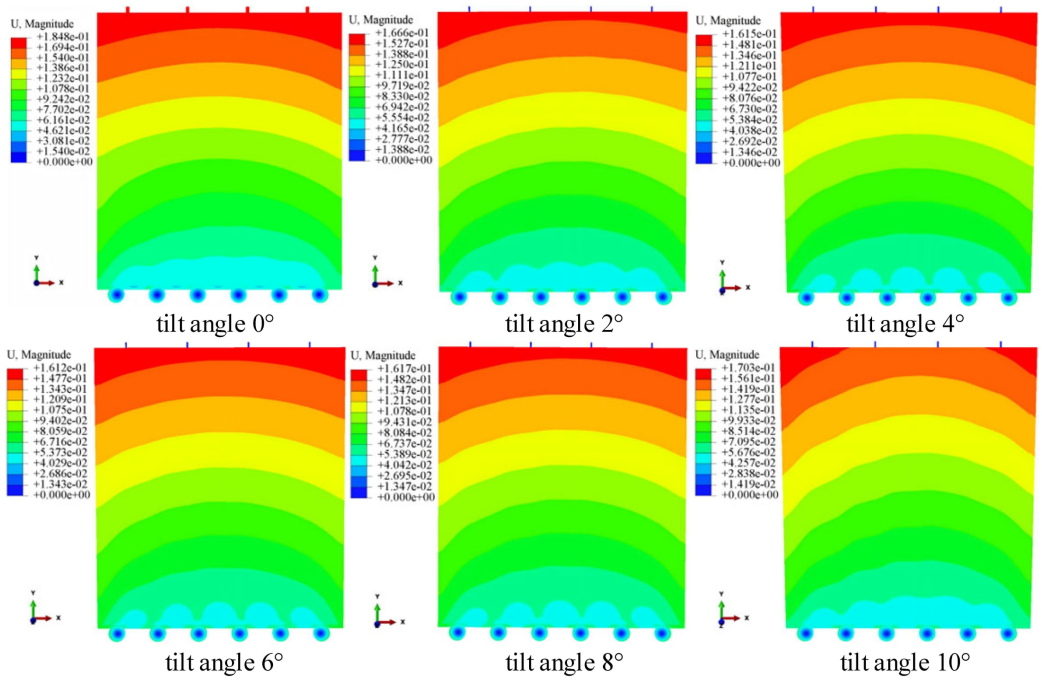


Figure 14. Overall forced-vibration displacement distributions of the large-size substrate at different tilt angles obtained by the modal superposition method.

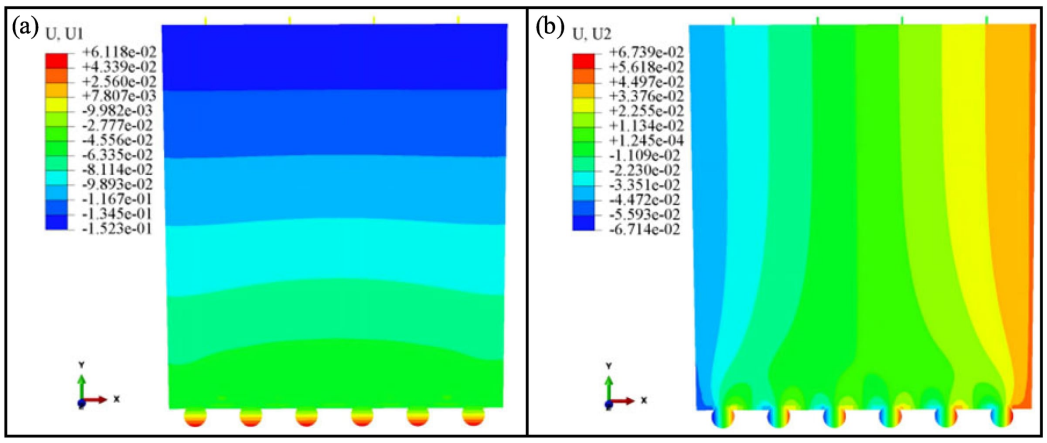


Figure 15. Forced-vibration displacement distributions at the optimal tilt angle of 6°: (**a**) X-direction response exhibiting a vertical spatial pattern; (**b**) Y-direction response exhibiting a horizontal spatial pattern.

Figure 16 illustrates the vibration displacement distribution of the large-size substrate at different tilt angles, obtained using the mode superposition method for forced vibration analysis. As the tilt angle increased, the displacement distribution remained horizontally oriented for all cases except the 0° condition. The displacement amplitudes at 0° and 2° were comparable; however, when the tilt angle increased beyond 4°, the amplitude decreased sharply and remained at a minimum value within the range of 4° to 6°. The displacement amplitude exhibited a strong dependence on the tilt angle. This finding highlights the significance of the gravitational component of the dynamic response in the Z-direction of the large-size substrate under tilt conditions.

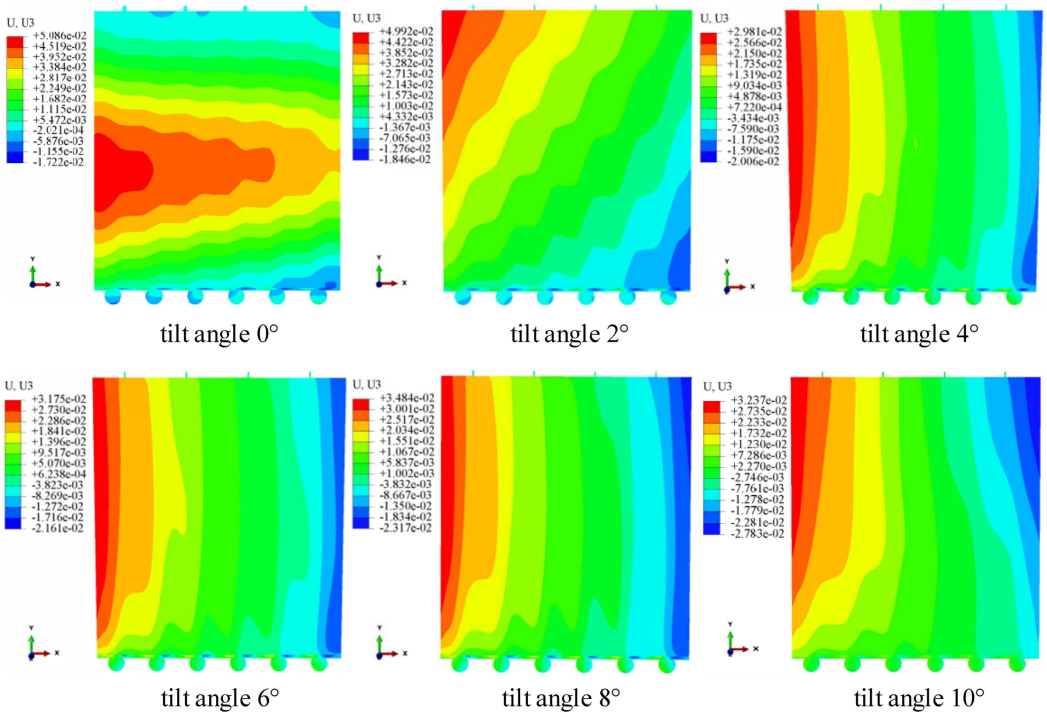


Figure 16. Z-direction forced-vibration displacement distributions of the large-size substrate at different tilt angles.

Figure 17 presents the forced vibration responses in each direction, obtained through modal superposition at a tilt angle of 6°. The superposition is dominated by the first and second modes, whereas the contributions from higher-order modes are negligible. Notably, the displacement, velocity, and acceleration distributions exhibit similar characteristics across different tilt angles. The overall mode shapes are dominated by bending deformation, with the response amplitude progressively increasing from the base to the top of the substrate. The mode shape in the X direction is mainly characterized by vertical deformation, whereas those in the Y and Z directions exhibit predominantly horizontal deformation characteristics.

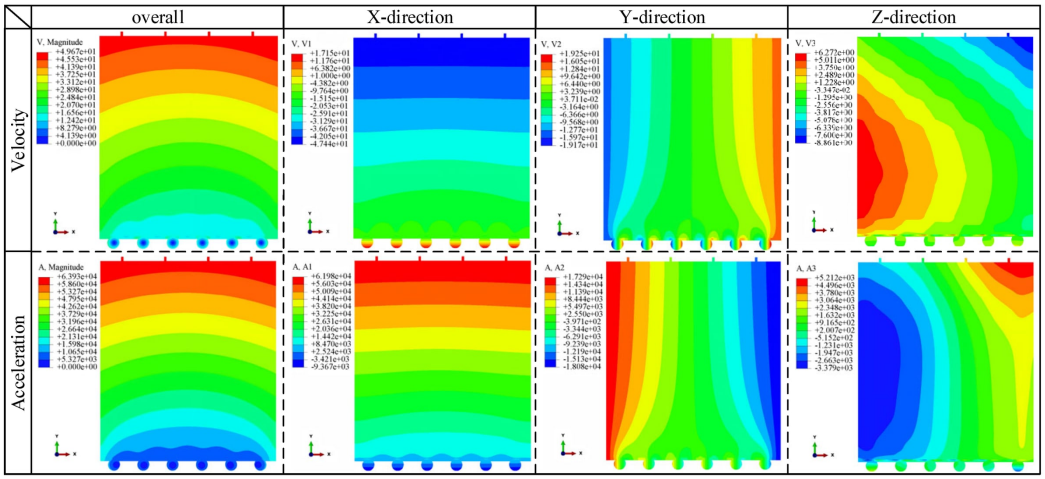


Figure 17. Forced-vibration dynamic responses of the large-size substrate at the optimal tilt angle of 6°.

3.1.5. Optimal Tilt Angle Analysis in the Tilt Mode

Figure 18 presents a statistical analysis of the dynamic response amplitudes and peak-to-peak values of the large-size substrate under tilt movement conditions in the different directions. The amplitude was largest in the X direction, followed by the Y direction, and smallest in the Z direction. The variation in amplitude, however, showed the opposite trend, with the largest fluctuation occurring in the Z direction. With respect to the vibration displacement, the X- and Y-direction amplitudes decreased slightly as the tilt angle increased, whereas the Z-direction displacement exhibited a non-monotonic variation characterized by an initial decrease followed by an increase. A pronounced reduction in vibration displacement was observed at a tilt angle of 6°. Relative to the 0° condition, the Z-direction amplitude and peak-to-peak value were reduced by 37.57% and 21.05%, respectively, indicating that an appropriate tilt angle can effectively suppress the vibration response of the substrate.

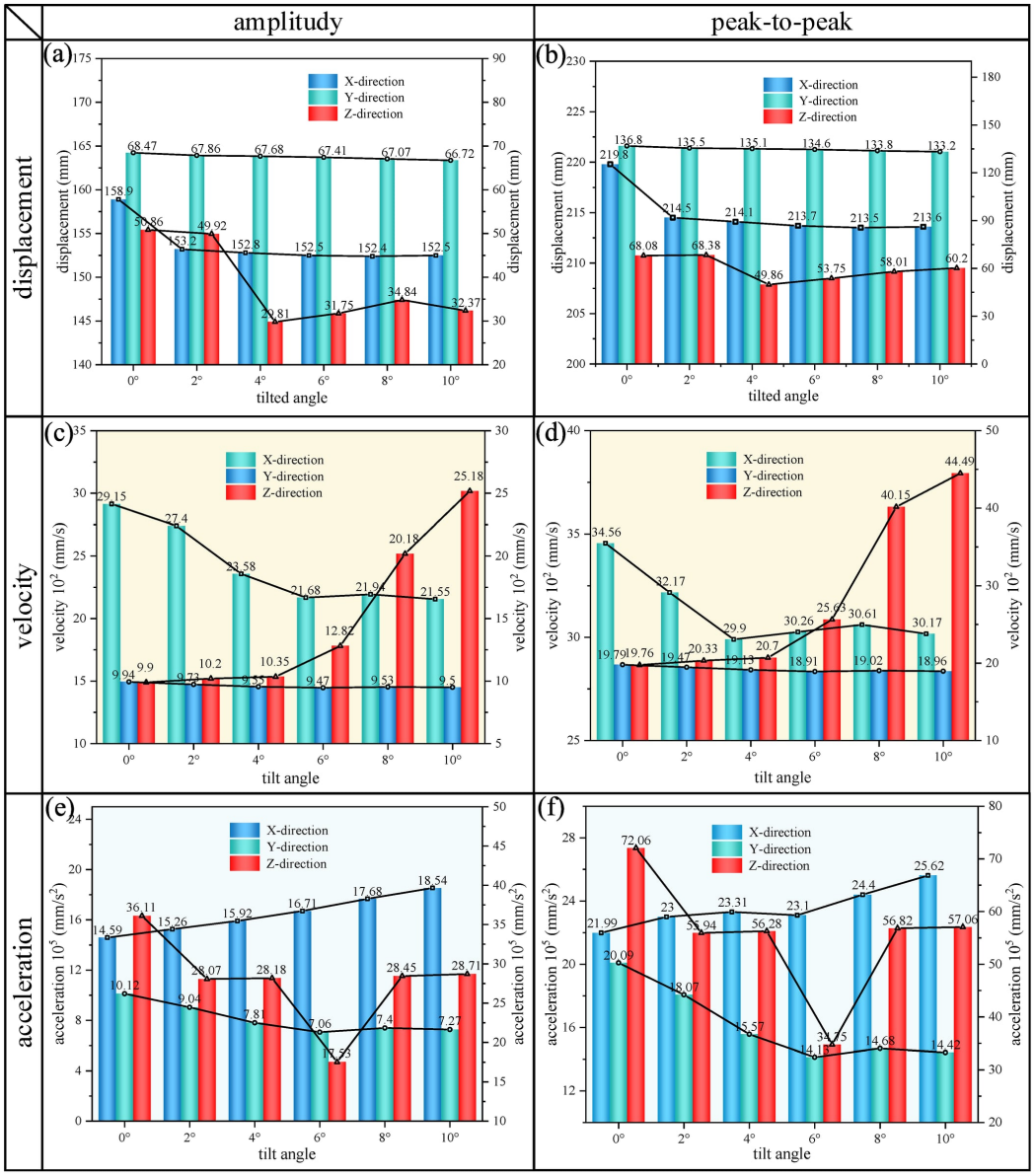


Figure 18. Comparison of the forced-vibration responses of the tilt movement system at various tilt angles: (**a**,**c**,**e**) amplitudes and (**b**,**d**,**f**) peak-to-peak values of (**a**,**b**) displacement, (**c**,**d**) velocity, and (**e**,**f**) acceleration.

With increasing tilt angle, the vibration velocities in the X- and Y-direction decreased slightly, whereas the velocity in the Z-direction exhibited an overall increasing trend. Nevertheless, a pronounced reduction in the velocity response was observed at a tilt angle of 6°. Compared with the 0° condition, the amplitude and peak-to-peak value in the X direction decreased by 25.6% and 12.4%, respectively; the corresponding reductions in the Y direction were 34.8% and 35.6%; while those in the Z direction were 4.7% and 4.5%. These results indicate that a tilt angle of 6° can effectively reduce the velocity response of the substrate, particularly in the X and Y directions. In terms of vibration acceleration, compared with the 0° condition, the amplitude and peak-to-peak value in the Z direction decreased by 13.4% and 13.9%, respectively, whereas the corresponding reductions in the Y direction were 51.5% and 51.8%. These results further demonstrate that the tilt angle effectively reduces the acceleration response of the substrate.

Overall, a tilt angle of 6° is recommended as the engineering optimum for vibration suppression. At this angle, the vibration velocity and acceleration in the X and Y directions, together with the vibration displacement and velocity in the Z direction, are consistently reduced, thereby improving the movement stability of the substrate. In contrast, the vibration reduction achieved at the other tilt angles is relatively limited. Furthermore, excessively large tilt angles enlarge the footprint of the magnetron sputtering system and lead to higher material consumption and manufacturing costs. Accordingly, taking both vibration suppression and engineering feasibility into account, a tilt angle of 6° is recommended.

The non-monotonic dependence of the vibration amplitude on the tilt angle arises from the competition between two effects: as the tilt angle increases, the gravitational component normal to the substrate surface increases, which raises the preload and geometric stiffness and modifies the load projection, reducing out-of-plane vibration; simultaneously, the in-plane gravitational component increases, which can induce additional bending deformation and compromise the coating uniformity. The optimal angle of 6 degrees represents the balance point where the stiffness and load-projection benefit is maximized before the detrimental bending effect becomes dominant. The abrupt changes observed in the fifth- and sixth-order mode shapes at 6 degrees (Figure 13) are attributed to the modal veering phenomenon, where two closely spaced modes exchange energy as the tilt angle modifies the stiffness distribution; this is a physical characteristic of the system rather than a numerical artifact, as confirmed by the consistent behavior across multiple mesh densities.

3.1.6. Refined Tilt-Angle Sampling and Verification of the Recommended Configuration

To assess the influence of tilt-angle sampling on the recommended configuration, additional forced-vibration analyses were performed at 5° and 7° and compared with the results at 6°. Material properties, support conditions, contact parameters, damping settings, and dynamic loading definitions were kept consistent across the three configurations. All vibration responses were calculated using the same modal superposition procedure.

Figure 19 presents the displacement contours at 5° and 7°, together with a comparison of the maximum resultant displacement at 5°, 6°, and 7°. As the tilt angle increased from 5° to 6°, the maximum resultant displacement decreased slightly from 161.5 to 161.2 μm, before returning to 161.5 μm at 7°. The 6° configuration therefore exhibited the lowest value among the three sampled angles, corresponding to a reduction of approximately 0.19% relative to both neighboring configurations. These results indicate a shallow local minimum at 6°.

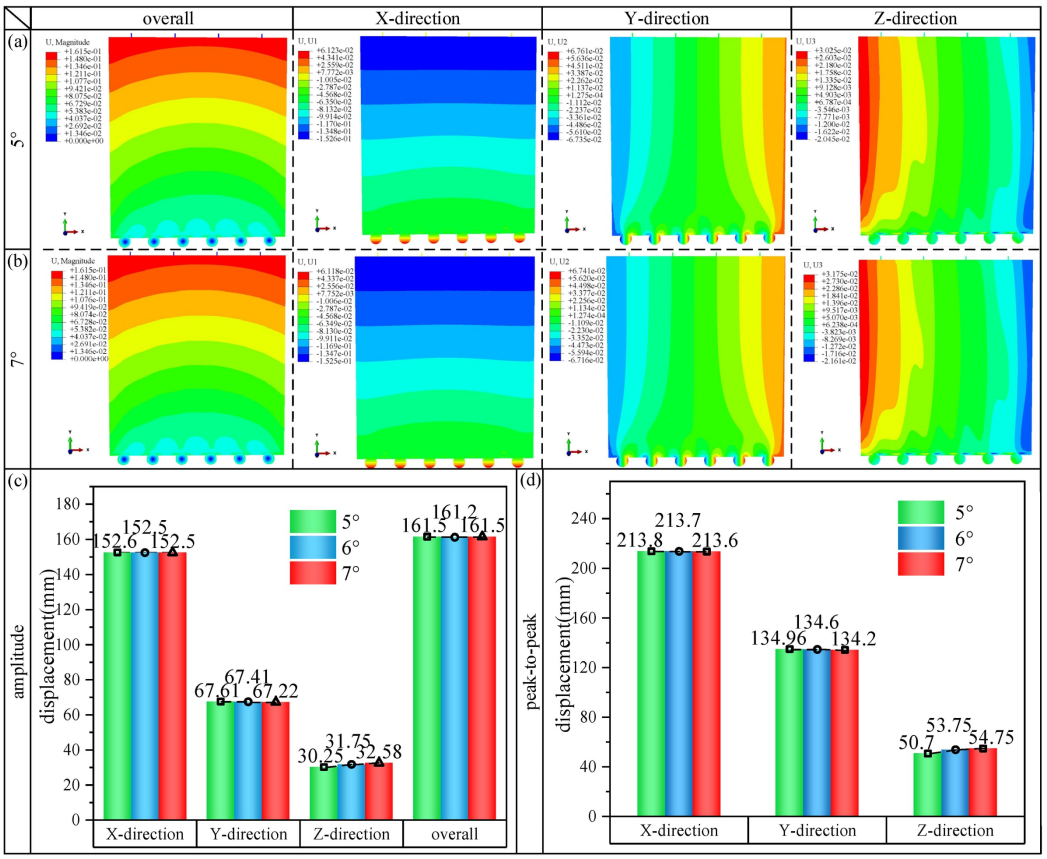


Figure 19. Comparison of vibration displacement at inclination angles of 5–7°: (**a**) 5°, (**b**) 7°, (**c**) amplitude, and (**d**) peak-to-peak.

The refined sampling provides a local consistency check for the previously recommended tilt angle. However, the maximum resultant displacements of the three configurations are closely comparable. This displacement comparison should therefore be considered alongside the other dynamic response measures discussed above when evaluating the suitability of the 6° configuration under the structural and excitation conditions investigated. Because the resultant-displacement margin is only 0.19%, this verification should be supplemented with Z-direction refinement over 4–8°; the 6° configuration is retained as an engineering recommendation rather than a sharp optimum.

3.2. Simulation Analysis in Vertical Mode

3.2.1. Free-Vibration Analysis of the Vertical Mode

The vertical mode was simulated following the same procedure as that used for the tilt mode, including the establishment of the corresponding simulation model. The primary difference lies in the boundary conditions, where an additional magnetic force was applied to the upper edge of the substrate in the vertical mode. Subsequently, the first six natural frequencies were calculated, as listed in Table 9.

Table 9. The first six natural vibration frequencies in vertical mode.

Order	1	2	3	4	5	6
Frequency (Hz)	19.99	167.43	526.13	570.41	969.96	1204.4

The vibration characteristics of the magnetic attraction positioning system located at the upper end of the substrate carrier were further investigated. Because one set of permanent magnets is fixed to the coating chamber housing, magnetic interaction occurs only when the permanent magnets mounted on the upper carrier are aligned with their corresponding counterparts on the chamber housing. The first six vibration modes of the complete substrate–carrier assembly were therefore computed to characterize the dynamic behavior of the vertical movement system.

It is worth noting that the first natural frequency of the vertical mode (19.99 Hz) is lower than that of the tilt mode (22.84 Hz), despite the additional magnetic constraint at the upper edge. This apparent contradiction is attributable to two factors. (1) The magnetic constraint acts only on the upper edge of the substrate carrier through non-contact magnetic coupling, which provides a restoring force but does not constitute a rigid fixed support. (2) The substrate carrier required by the vertical mode adds substantial mass to the system. The combined effect is a reduction in the effective stiffness-to-mass ratio and hence a lower fundamental frequency. Nevertheless, the magnetic constraint effectively suppresses the forced-vibration response amplitude, as demonstrated in Section 3.2.3, because it provides additional positional confinement and a restoring force during movement.

Figure 20 illustrates the first six vibration modes of the large-size substrate in the vertical mode. The overall mode distributions exhibited distinct distribution characteristics for different mode orders. As the mode order increased, the mode shapes became progressively more complex, gradually evolving from predominantly vertical to horizontal distributions. In particular, the fifth and sixth modes exhibited pronounced local responses. The mode shapes in the Z direction were highly consistent with those in the overall direction, whereas those in the X- and Y-directions were negligible. These results indicate that the Z direction remains the dominant vibration direction in both the tilt and the vertical modes.

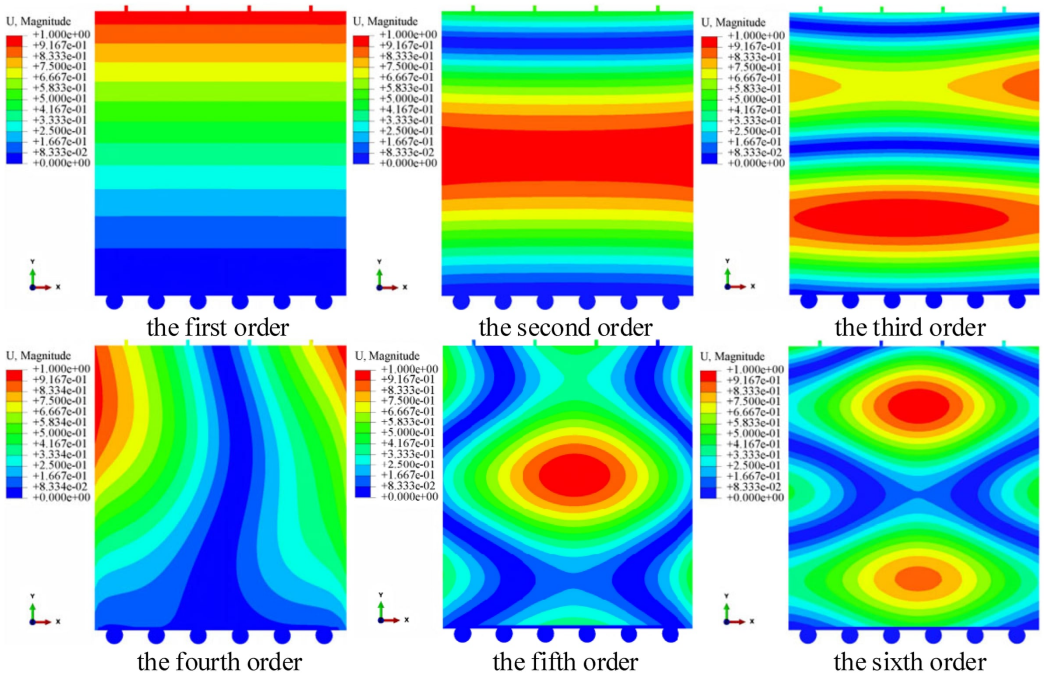


Figure 20. The first six overall free-vibration mode shapes of the complete substrate-carrier assembly in the vertical movement mode.

3.2.2. Forced-Vibration Analysis of the Vertical Mode

Following the same procedure adopted for the tilt mode, a forced-vibration mode superposition analysis was conducted using the first six free-vibration modes, including their natural frequencies and corresponding mode shapes. The modal effective mass distribution for the vertical mode was subsequently obtained, as summarized in Table 10. Unlike the tilt mode, the first-order mode was identified as the primary contributor to the modal effective mass, while the fourth-order mode served as the secondary contributor. Collectively, these two modes account for 96.65% of the total modal effective mass, whereas the contributions of the remaining modes are negligible.

Table 10. Modal effective mass proportion of the vertical mode.

Order	1	2	3	4	5	6
Effective mass proportion (%)	81.75	0.16	2.04	14.90	<0.01	1.14

Figure 21 shows the forced vibration response of the large-size substrate in the vertical mode, obtained using the modal superposition method. The effective mass analysis indicates that the first and fourth modes dominate all forced vibration responses, including those of displacement, velocity, and acceleration, whereas the higher-order modes contributed only minor local fluctuations near the drive roller and had a negligible influence on the overall substrate response.

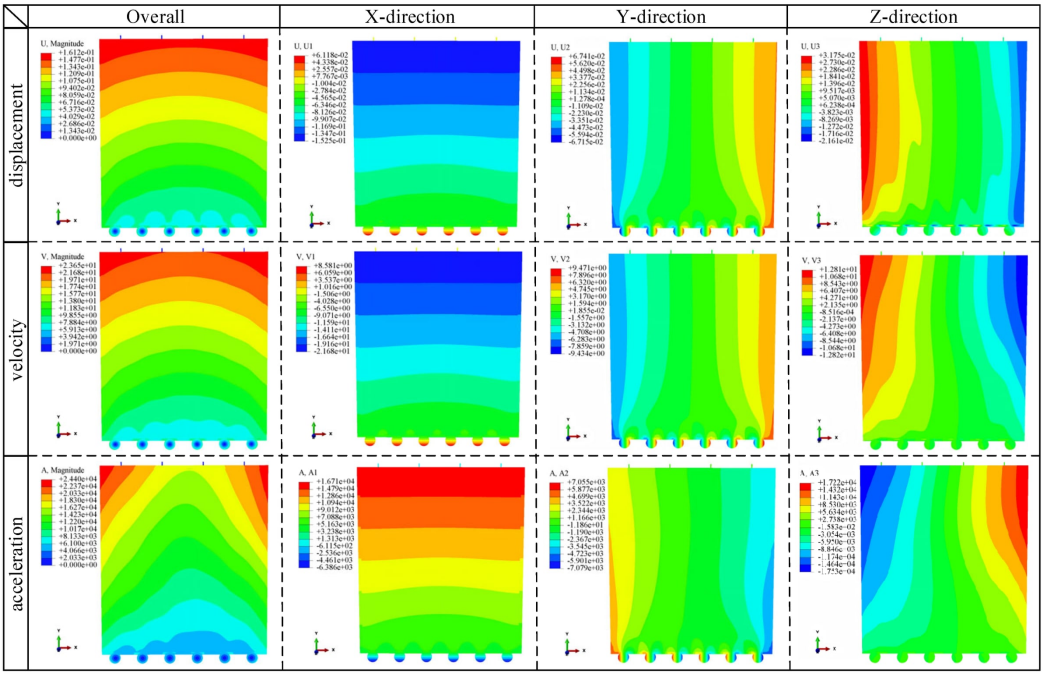


Figure 21. Forced-vibration responses of the large-size substrate in the vertical movement mode obtained by modal superposition.

The displacement, velocity, and acceleration exhibited highly consistent spatial contributions, with all three response quantities displaying similar modal characteristics. A pronounced gradient was observed along the vertical direction of the substrate, with the maximum response occurring in the upper region of the structure, and the minimum amplitude located near the bottom region constrained by the drive wheel. This distribution is highly consistent with the characteristics of low-order bending modes. For the responses in the X- and Y-directions, the modal patterns of dynamic amplitudes remain essentially

unchanged, predominantly characterized by vertical and horizontal distribution features, respectively. In contrast, in the Z-direction, which serves as the dominant vibration direction in the vertical mode, the dynamic response exhibits a consistent evolution pattern characterized by horizontally distributed arc-shaped contours extending across the substrate. In addition, the acceleration amplitude shows a noticeable local increase in the upper-right region of the substrate. The velocity and acceleration fields in all three directions closely correspond to their respective displacement fields, demonstrating a high degree of consistency in the overall modal patterns. This agreement is expected because displacement, velocity, and acceleration are linearly related under steady-state harmonic forced vibration. These results further confirm that the forced vibration response is governed primarily by the superposition of the dominant vibration modes.

3.2.3. Comparative Analysis of the Vertical and Tilt Modes

Based on the preceding analyses, the vertical mode provides superior performance in enhancing the movement stability of large-size substrates. To further evaluate its dynamic characteristics, a comparative analysis of the vibration responses under modal superposition conditions was conducted, with particular emphasis on the influence of the Z-direction responses of the vertical and tilt modes on the overall dynamic behavior of the system.

Figure 22 compares the maximum vibration displacements of the substrate in terms of the overall response and the Z-direction response under forced-vibration modal superposition for the two movement modes. For comparison, the modal superposition results for the tilt mode at different tilt angles are also presented, with the 6° tilt mode serving as the optimized baseline and the 0° condition as the un-tilted reference. As shown in Figure 22a,b, the introduction of magnetic force reduces the overall vibration displacement of the substrate. Relative to the 0° tilt mode, the vertical mode decreases the overall amplitude by 15.8%, and a further reduction of 3.47% is achieved relative to the 6° tilt mode. On the coating-critical Z-direction component, however, the vertical mode remains approximately 51% higher than the 6° tilt mode, because the magnetic constraint strongly suppresses the lateral X- and Y-responses but restrains the out-of-plane bending only weakly. Relative to the 0° tilt condition, the vertical mode reduces the Z-direction amplitude by 5.92% and the peak-to-peak value by 5.14%. These results indicate that the magnetic constraint enhances the overall and lateral dynamic stability, whereas the optimized tilt mode provides better control of the coating-critical Z-direction response. The practical implementation of the vertical mode is nevertheless associated with certain limitations, including relatively low utilization efficiency of the substrate carrier, together with increased maintenance requirements and higher energy consumption during long-term operation. The selection of an appropriate movement mode should therefore be based on a comprehensive evaluation of dynamic performance, energy efficiency, maintenance requirements and operating cost in accordance with the specific production requirements.

The difference in magnitude between the overall reduction (15.8%) and the Z-direction reduction (5.92%) follows directly from the directional composition of the response. In the un-tilted tilt mode, the absolute X- and Y-direction displacement amplitudes are larger than the Z-direction amplitude (Section 3.1.5), although the Z-direction out-of-plane bending governs the modal deformation and the target–substrate distance variation. The magnetic attraction constraint acts mainly on the upper edge of the carrier and strongly suppresses the lateral X- and Y-direction components, whereas its restoring effect in the out-of-plane Z-direction is comparatively weak, so that the Z-direction amplitude decreases by only 5.92%. Because the overall amplitude is a composite of all three directional components, the strong suppression of the X and Y components produces the 15.8% overall reduction, while the coating-critical Z-direction achieves a smaller but still positive improvement relative to

0°. Relative to the 6° tilt configuration, however, the vertical Z-direction amplitude remains about 51% larger; the vertical mode is therefore superior in overall and lateral terms but not on the coating-critical Z component.

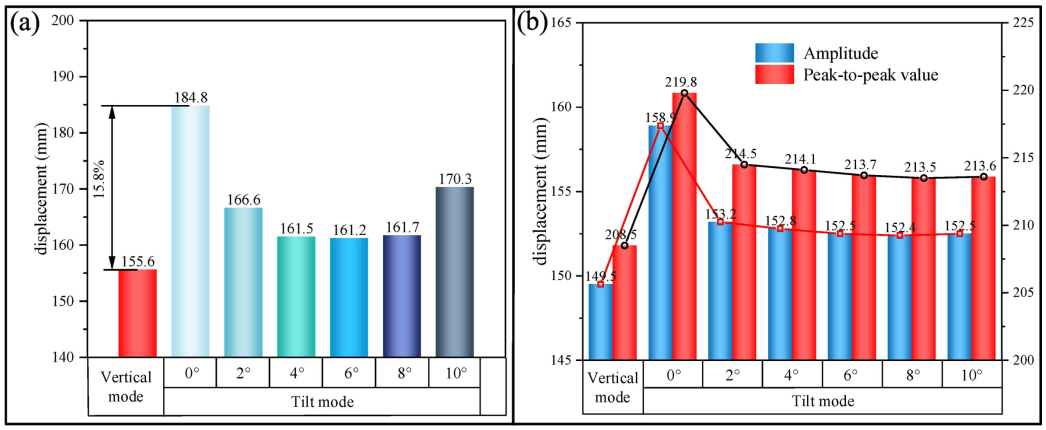


Figure 22. Maximum vibration displacements of the large-size substrate: (**a**) overall; (**b**) Z-direction.

The relationship between the observed vibration characteristics and the actual film coating performance merits further discussion. In magnetron sputtering, the thickness uniformity of the deposited film is governed directly by the relative distance and angle between the target and the substrate surface. The out-of-plane vibration in the Z direction, identified as the dominant vibration mode in both movement configurations, induces periodic fluctuations in the target–substrate distance. Relative to the 0° tilt condition, the 5.92% reduction in Z-direction amplitude is expected to diminish the thickness non-uniformity induced by distance variation, whereas relative to the 6° tilt configuration the vertical mode exhibits a larger Z-direction motion and is not expected to improve uniformity. These effects are anticipated but have not been verified experimentally. Furthermore, the vibration frequency and acceleration influence the residual stress state of the growing film: higher acceleration amplitudes can induce microstructural disturbances during atom deposition, potentially increasing the residual stress and reducing film adhesion. The vertical mode reduces the overall response amplitude by 15.8% relative to 0° (and by 3.47% relative to 6°), so an overall improvement in stability and residual stress is expected for high-precision optical and electronic coatings, pending direct experimental validation. Although direct experimental validation of the film properties lies beyond the scope of the present simulation study, the established correlation between dynamic response amplitude and coating quality provides a physically meaningful basis for movement mode selection.

Figure 22. Comparison of the maximum forced-vibration displacement between the vertical mode and the tilt mode at various tilt angles: (a) overall response; (b) dominant Z-direction response, quantifying the 15.8% overall amplitude reduction and the 5.92% Z-direction amplitude reduction achieved by the magnetic constraint.

3.2.4. Mechanism Difference and Application Scenario Comparison

The performance difference between the two configurations originates in their distinct vibration suppression mechanisms. The carrier-free tilt mode relies on the normal component of gravity to increase the contact preload at the rollers and to modify the geometric stiffness of the thin plate; it primarily suppresses the out-of-plane (Z-direction) bending vibration, which directly determines the target–substrate distance variation and hence the coating thickness uniformity. The permanent-magnet constrained vertical mode provides a non-contact restoring force at the upper edge of the carrier and primarily suppresses the

in-plane (X/Y direction) rigid-body displacement and swing, which dominate the lateral positioning accuracy of the substrate.

From an engineering application perspective, the two configurations are complementary rather than mutually superior. The 6° tilt mode is preferred for production lines focused on coating thickness uniformity, such as single-sided optical and functional oxide coating systems, and it additionally offers the advantages of no carrier, a simple structure, low equipment cost and high chamber space utilization. The vertical mode is more suitable for scenarios with high requirements on lateral positioning accuracy and double-sided coating alignment, such as double-sided transparent conductive glass deposition lines, although its carrier structure results in higher manufacturing and maintenance costs and lower space utilization.

Compared with existing studies, which focus mainly on deposition process optimization and robotic handling between chambers, this study addresses the substrate dynamic behavior during in-chamber transport for G10.5 large-size substrates and provides quantitative guidance for transport system design.

4. Conclusions

This study investigated the dynamic characteristics of large-size-substrate movement systems under two movement configurations, namely, the tilt movement mode and the vertical mode. Free- and forced-vibration modal analyses were performed to evaluate the dynamic responses of both configurations, and the forced-vibration responses were obtained using the mode superposition method. The objective defined in the Introduction—quantifying and comparing the dynamic performance of the two substrate movement modes to guide mode selection—has been achieved. The principal conclusions are summarized as follows.

1. Through theoretical calculations combined with static mechanical analysis, the maximum allowable tilt angle of the tilt movement mode was determined to be below 10°, based on the coating uniformity requirement that the maximum substrate deflection must not exceed 0.34 mm.
2. The first six natural modes of the tilt mode exhibit distinct directional characteristics: the X-direction mode displays an up–down pattern, the Y-direction mode a left–right pattern, and the Z-direction mode transitions from up–down to left–right with increasing mode order. The Z direction was identified as the dominant vibration direction in both movement configurations.
3. The forced-vibration results of the tilt mode were evaluated using a modal superposition approach. Among the investigated angles, 6° provides the best vibration suppression performance. At this angle, the vibration velocity and acceleration amplitudes, together with the peak-to-peak values in the X and Y directions, and the displacement and velocity amplitudes, together with the peak-to-peak values in the Z direction, were effectively reduced. Taking both the dynamic performance and the increase in system footprint and material cost associated with large tilt angles into account, we recommend an angle of 6° for large-size-substrate movement systems.
4. The dynamic characteristics of the vertical mode were further analyzed through free- and forced vibration analyses. Compared with the tilt mode, the introduction of magnetic constraint consistently improved the overall and lateral dynamic stability of the movement system. Relative to the tilt mode at 0 degrees, the overall displacement amplitude was reduced by 15.8%, with the Z-direction amplitude and peak-to-peak value decreased by 5.92% and 5.14%, respectively. Relative to the optimized tilt mode at 6 degrees, the overall amplitude was further reduced by 3.47%. On the coating-critical Z-direction component, however, the vertical mode remained approximately 51% above

the tilt mode at 6°; the 6° tilt mode is therefore recommended where coating uniformity is the controlling requirement, whereas the vertical mode is preferred where lateral positional stability dominates.

The two modes provide complementary advantages: the vertical mode offers superior overall and lateral vibration suppression, whereas the 6° tilt mode provides better control of the coating-critical Z-direction response. The vertical mode is also constrained by the need for an additional substrate support structure, which leads to higher installation and maintenance costs and low equipment utilization. The selection should therefore be based on a comprehensive evaluation of dynamic performance, production requirements, energy consumption and economic cost. The present study provides a useful theoretical basis and engineering reference for the design and optimization of movement methods for large-size substrates. In particular, this study offers the first quantitative comparison of substrate dynamic behavior at the G10.5 scale, linking the panel's vibration response directly to coating-relevant movement performance.

It should be acknowledged that the conclusions of this study are derived from theoretical analysis and finite-element numerical simulation, and experimental validation has not yet been performed. Future work will focus on two aspects. (1) A prototype movement test rig equipped with laser displacement sensors and accelerometers will be constructed to measure experimentally the vibration response of large-size substrates under both the tilt and vertical configurations, thereby validating the predicted natural frequencies, the optimal tilt angle and the relative damping performance. (2) Comparative coating experiments will be conducted to characterize the film thickness uniformity, residual stress and adhesion strength achieved under each movement mode, which will establish directly the quantitative relationship between substrate dynamic behavior and coating quality. Such experimental validation will further strengthen the practical applicability of the proposed movement modes.

Practical Implications for Engineering

The findings provide direct guidance for the design of large-size magnetron sputtering production lines. For coating processes in which thickness uniformity is the core index, the carrier-free 6° tilt transport mode is recommended, which effectively reduces out-of-plane vibration and improves coating quality without additional carrier cost. For processes requiring high lateral positioning accuracy and double-sided coating alignment, the permanent-magnet constrained vertical mode is recommended to obtain better overall transport stability.

The analysis framework and modeling method established in this study can be extended to the dynamic design of other large-area thin-plate vacuum transport systems.

Author Contributions: L.H.: Conceptualization (lead); methodology (lead); software (lead); writing—original draft (lead); and writing—review & editing (lead). Q.Z.: Formal analysis (lead); investigation (lead); resources (lead); writing—original draft (equal); and writing—review & editing (equal). C.H.: Data curation (equal); investigation (equal); supervision (equal); and writing—review & editing (equal). X.W.: Funding acquisition (equal); investigation (equal); and validation (equal). S.L.: Software (supporting); writing—original draft (supporting); and writing—review & editing (supporting). All authors have read and agreed to the published version of the manuscript.

Funding: This research was funded by the Excellent Youth Project of Education Department of Hunan Province (No. 25B0162) and the Hunan Provincial Science and Technology Innovation Plan-Innovative Talent Plan-Huxiang Youth Talent Project of Science and Technology Innovation (No. 2024RC3278).

Data Availability Statement: The original contributions presented in this study are included in the article. Further inquiries can be directed to the corresponding author.

Acknowledgments: The authors thank Xiangtan Hongda Vacuum Technology Co., Ltd., for providing the equipment drawings and process parameters used in this study.

Conflicts of Interest: Author Le Huang was employed by the Xiangtan Hongda Vacuum Technology Co., Ltd. The remaining authors declare that the research was conducted in the absence of any commercial or financial relationships that could be construed as a potential conflict of interest.

Abbreviations

Symbol	Meaning
δV, δS	volume, surface magnetization current density
B, B_r	magnetic, remanence flux density
B_x, B_y, B_z	the magnetic flux density in the x, y, z direction
S	magnetic pole area
S_A, S_B, S'_A, S'_B	N-pole, S-pole surfaces
μ_0, μ_r	vacuum, permanent magnet permeability
M_0, M	medium, intensity magnetization
r_i	distance (the magnetic charge element on the pole surface to the spatial point Q)
σ_m	surface magnetic charge density
n	surface normal vector
q	charge of positive ions
V_t, V_x	cathode, positive-ion voltage
E_{Ar},E_{con}	positive-ion energy, binding energy of target atom
E_b	the energy loss during the cascade process
E_d	the lost energy (the working gas ionization)
K_b	Boltzmann constant
T	operating temperature
d_g	the molecular diameter of the working gas
L	substrate length
b	substrate width
t	substrate thickness
G	substrate weight
θ	tilt angle

References

1. Borowski, P.; Myśliwiec, J. Recent Advances in Magnetron Sputtering: From Fundamentals to Industrial Applications. *Coatings* **2025**, *15*, 922. [CrossRef]
2. Zhong, H.; Härtel, M.S.; Chen, W.; Spanier, L.V.; Yin, S.; Zhang, J.; Seibertz, B.B.O.; Szyszka, B.; Albrecht, S.; Schwartzkopf, M. In Situ GISAXS Study of IZO Deposition via Magnetron Sputtering for Optoelectronic Devices: Film Growth and Ion Bombardment-Induced Degradation Dynamics. *Adv. Sci.* **2026**, *13*, e16853. [CrossRef]
3. Seyhan, A.; Kartal, E. Optical, electrical and structural properties of ITO/IZO and IZO/ITO multilayer transparent conductive oxide films deposited via radiofrequency magnetron sputtering. *Coatings* **2023**, *13*, 1719. [CrossRef]
4. Murzin, S.P. Artificial Intelligence-Guided Pulsed Synthesis of Zinc Oxide Nanostructures on Thin Metal Shells. *Processes* **2025**, *13*, 3755. [CrossRef]
5. Lin, S.-H.; Chang, Y.-H.; Huang, Y.-J.; Chen, Y.-T.; Dong, S.-H. Annealing Temperature Effect on the Properties of CoCe Thin Films Prepared by Magnetron Sputtering at Si(100) and Glass Substrates. *Processes* **2024**, *12*, 2806. [CrossRef]
6. Álvarez-Fraga, L.; Gago, R.; Araiza, J.d.J.; Azpeitia, J.; Jiménez, I.; Sánchez, O. Impact of Silver on the Structural and Wettability Properties of ZnO Films Grown by Oblique Angle Magnetron Sputtering. *Processes* **2023**, *11*, 1428. [CrossRef]
7. Zhou, X.; Lan, Y.; Cai, J.; Chen, J.; Min, J. Preparation and thermal stability of Mo/AlMoONH/AlMoONL/AlxOy solar selective absorption coatings. *J. Vac. Sci. Technol. A* **2026**, *44*, 043101. [CrossRef]
8. Sidelev, D.V.; Voronina, E.D.; Bleykher, G.A. Reactive magnetron sputtering of copper oxide coatings using the metallic mode assisted by RF-ICP source: Experiment and calculation. *J. Vac. Sci. Technol. A* **2026**, *44*, 013403. [CrossRef]
9. Lv, Z.; Shen, X.; Guo, J.; Cao, Y.; Lan, C.; Ke, Y.; Yang, Y.; Qi, J. Microstructure and Magnetic Properties Dependence on the Sputtering Power and Deposition Time of TbDyFe Thin Films Integrated on Single-Crystal Diamond Substrate. *Processes* **2022**, *10*, 2626. [CrossRef]
10. Mydłowska, K.; Czerwińska, E.; Gilewicz, A.; Dobruchowska, E.; Jakubczyk, E.; Szparaga, Ł.; Ceynowa, P.; Ratajski, J. Evolution of Phase Composition and Antibacterial Activity of Zr–C Thin Films. *Processes* **2020**, *8*, 260. [CrossRef]

11. Tu, R.; Qin, Z.; Wu, W.; Zheng, L.; Xu, Q.; Gao, T.; Zhang, S.; Dai, H.; Goto, T. Corrosion resistance and antimicrobial properties of ZnO-Ce2O3 coatings by magnetron sputtering. *J. Vac. Sci. Technol. A* **2025**, *43*, 043406. [CrossRef]
12. Kozelskaya, A.I.; Maryin, P.V.; Sosnina, A.V.; Rutkowski, S.; Shugurov, A.R.; Zhukov, Y.; Tran, H.T.; Bukal, V.R.; Akimchenko, I.O.; Nasibov, T.F. Effect of argon and nitrogen mixing ratios on the properties of the coatings deposited via reactive magnetron sputtering of a hydroxyapatite target. *Appl. Surf. Sci.* **2026**, *726*, 165972. [CrossRef]
13. Kipkirui, N.G.; Lin, T.-T.; Kiplangat, R.S.; Lee, J.-W.; Chen, S.-H. HiPIMS and RF magnetron sputtered Al0. 5CoCrFeNi2Ti0. 5 HEA thin-film coatings: Synthesis and characterization. *Surf. Coat. Technol.* **2022**, *449*, 128988.
14. Psiuk, R.; Mościcki, T.; Chrzanowska-Giżyńska, J.; Kurpaska, Ł.; Radziejewska, J.; Denis, P.; Garbiec, D.; Chmielewski, M. Mechanical and thermal properties of W-Ta-B coatings deposited by high-power impulse magnetron sputtering (HiPIMS). *Materials* **2023**, *16*, 664. [CrossRef]
15. Xu, Y.; Zhang, J.; Liang, F.; Yin, M.; He, M. Investigation of magnetron sputtered nano-silver coating on titanium surface with micro-nanostructure. *Surf. Interfaces* **2023**, *38*, 102770. [CrossRef]
16. Ma, P.; Liu, Y.; Cao, L.; Zhang, Y.; Li, X.; Tian, W.; Qiu, S.; Su, G. In-situ TEM Study of Dislocation Loop Evolution in Tungsten under Dual-ion Beam Irradiation. *Nucl. Eng. Technol.* **2025**, *59*, 874–883.
17. Liu, Y.; Zhu, S.; Song, B. Optical and Electrical Properties of Transparent Conductive NTTO/Cu/NTTO Multilayer Films Deposited by Magnetron Sputtering. *JOM* **2019**, *71*, 3720–3726. [CrossRef]
18. Yurjev, Y.; Savelev, A.; Yurjeva, A.; Kazimirov, A.; Kharisova, A. Deposition of superconducting nb3sn coatings using multiple magnetron sputtering techniques. *Metals* **2023**, *13*, 1730. [CrossRef]
19. Graiser, S.; Taylor, G.V.; Aji, L.B.; Shin, S.; Goodelman, D.; Sohngen, L.; Merlo, J.; Chavez, X.L.; Kucheyev, S. Effects of substrate bias and tilt on magnetron sputtered boron carbide films. *Diam. Relat. Mater.* **2025**, *160*, 112992. [CrossRef]
20. Tian, G.; Li, X.; Chai, P.; Wang, Y. Effect of deposition angle on the deposition rate, microstructure, electrical and optical properties of magnetron sputtered ZrB2 thin films. *Mater. Lett.* **2023**, *348*, 134696. [CrossRef]
21. Engwall, A.; Aji, L.B.; Baker, A.; Shin, S.; Bae, J.; McCall, S.; Moody, J.; Kucheyev, S. Effect of substrate tilt on sputter-deposited AuTa films. *Appl. Surf. Sci.* **2021**, *547*, 149010. [CrossRef]
22. Schlichting, F.; Thormaehlen, L.; Cipo, J.; Meyners, D.; Kersten, H. Energy-dependent film growth of Cu and NiTi from a tilted DC magnetron sputtering source determined by calorimetric probe analysis. *Surf. Coat. Technol.* **2022**, *450*, 129000. [CrossRef]
23. Huang, H.; Jiang, L.; Yao, Y.; Zhang, Z.; Wang, Z.; Qi, R. Controlling film thickness distribution by magnetron sputtering with rotation and revolution. *Coatings* **2021**, *11*, 599. [CrossRef]
24. Ayachi Omar, A.; Luchkin, A.G.; Alsayed Omar, M.R.; Kashapov, N.F. The effect magnet design on controlling the target erosion profile for DC magnetron with the rectangular target. *Plasma Chem. Plasma Process.* **2023**, *43*, 361–379. [CrossRef]
25. Jo, Y.H.; Park, H.S.; Hur, M.Y.; Lee, H.J. Curved-boundary particle-in-cell simulation for the investigation of the target erosion effect of DC magnetron sputtering system. *AIP Adv.* **2020**, *10*, 125224. [CrossRef]
26. Engwall, A.; Aji, L.B.; Shin, S.; Baker, A.; Bae, J.; McCall, S.; Moody, J.; Kucheyev, S. Sputter deposition of high electrical resistivity Au-Ta alloy coatings on rotating substrates. *Thin Solid Films* **2022**, *758*, 139411. [CrossRef]
27. Fungfuang, N.; Khlayboonme, S.T.; Kitiwan, M. Effects of substrate rotational speed and phase transition on β-V2O5 for temperature-sensitive thin films. *Opt. Laser Technol.* **2025**, *191*, 113296. [CrossRef]
28. Tang, J.-F.; Huang, C.-H.; Lin, C.-Y.; Yang, F.-C.; Chang, C.-L. Effects of substrate rotation speed on structure and adhesion properties of CrN/CrAlSiN multilayer coatings prepared using high-power impulse magnetron sputtering. *Coatings* **2020**, *10*, 742. [CrossRef]
29. Lasseur, V.; Goutier, S.; Martinez Garcia, V.; Denoirjean, A.; Meillot, E.; Mariaux, G.; Absi, J.; Killinger, A. Residual stress evolution in zirconia (Y8%) coatings during atmospheric plasma spraying for substrates under rotating kinematic. *J. Therm. Spray Technol.* **2020**, *29*, 1313–1321. [CrossRef]
30. Chen, S.; Sun, J.; Li, J.; Yi, K.; Wang, C.; Shao, J.; Zhu, M. Controlling lateral thickness distributions of magnetron sputtering deposited coatings using shadow masks. *Opt. Mater. Express* **2023**, *14*, 101–115. [CrossRef]
31. Liu, X.; Zhang, Z.; Song, H.; Huang, Q.; Huo, T.; Zhou, H.; Qi, R.; Zhang, Z.; Wang, Z. Comparative study on microstructure of Mo/Si multilayers deposited on large curved mirror with and without the shadow mask. *Micromachines* **2023**, *14*, 526. [CrossRef]
32. Zhang, Z.; Qi, R.; Yao, Y.; Shi, Y.; Li, W.; Huang, Q.; Yi, S.; Zhang, Z.; Wang, Z.; Xie, C. Improving thickness uniformity of Mo/Si multilayers on curved spherical substrates by a masking technique. *Coatings* **2019**, *9*, 851. [CrossRef]
33. Li, T.-C.; Li, D.-L.; Ho, J.; Yu, C.-C.; Wang, S.-S.; Ho, J.-J. Enhancing Thickness Uniformity of Nb2O5/SiO2 Multilayers Using Shadow Masks for Flexible Color-Filtering Applications. *Micromachines* **2024**, *15*, 551. [CrossRef]
34. Liu, Z.; Chen, Y.; Song, H.; Xing, Z.; Tian, H.; Shan, X. High-Speed Handling Robot with Bionic End-Effector for Large Glass Substrate in Clean Environment. *Sensors* **2022**, *22*, 149. [CrossRef]
35. Shan, X.; Song, H.; Zhang, C.; Wang, G.; Fan, J. Linear System Identification and Vibration Control of End-Effector for Industrial Robots. *Appl. Sci.* **2020**, *10*, 8537. [CrossRef]

36. Liu, C.; Chen, Y. Combined S-Curve Feedrate Profiling and Input Shaping for Glass Substrate Transfer Robot Vibration Suppression. *Ind. Robot* **2018**, *45*, 549–560. [CrossRef]
37. Seo, J.-H.; Hwang, J.-C.; Choi, Y.-W.; Yim, H.-J. Analysis and Design Study of LCD Transfer Robot Using Dynamic Simulation and Experiment. *J. Mech. Sci. Technol.* **2009**, *23*, 1035–1039. [CrossRef]
38. *SEMI D5*; Standard Sizes for Flat Panel Display Substrates. SEMI International: San Jose, CA, USA, 2003.
39. *SEMI D15*; FPD Glass Substrate Surface Waviness Measurement Method. SEMI International: San Jose, CA, USA, 2003.
40. *Standard's ASTM A29/A29M-24; Standard*; Specification for Steel Bars, Carbon and Alloy, Hot-Wrought, General Requirements for. ASTM International: West Conshohocken, PA, USA, 2024.

Disclaimer/Publisher's Note: The statements, opinions and data contained in all publications are solely those of the individual author(s) and contributor(s) and not of MDPI and/or the editor(s). MDPI and/or the editor(s) disclaim responsibility for any injury to people or property resulting from any ideas, methods, instructions or products referred to in the content.